
MULTI-SCALE PHYLODYNAMIC MODELLING OF RAPID PUNCTUATED PATHOGEN EVOLUTION

Quang Dang Nguyen*
Centre for Complex Systems
Faculty of Engineering
The University of Sydney, Australia

Sheryl L. Chang*
Centre for Complex Systems
Faculty of Engineering
The University of Sydney, Australia
sheryl.chang@sydney.edu.au

Carl J. E. Suster
Centre for Infectious Diseases and
Microbiology–Public Health
Westmead Hospital
NSW, Australia

Rebecca J. Rockett
Centre for Infectious Diseases and
Microbiology–Public Health
Westmead Hospital
NSW, Australia

Vitali Sintchenko
Sydney Infectious Diseases Institute
The University of Sydney
NSW, Australia

Tania C. Sorrell
Sydney Infectious Diseases Institute
The University of Sydney
NSW, Australia

Mikhail Prokopenko
Centre for Complex Systems
Faculty of Engineering
The University of Sydney, Australia

December 10, 2024

ABSTRACT

Computational multi-scale pandemic modelling remains a major and timely challenge. Here we identify specific requirements for a new class of pandemic models operating across three scales: (1) rapid pathogen evolution, punctuated by emergence of new variants, (2) human interactions within a heterogeneous population, and (3) public health responses which constrain individual actions to control the disease transmission. We then present a pandemic modelling framework satisfying these requirements and capable of simulating multi-scale dynamic feedback loops. The developed framework comprises a stochastic agent-based model of pandemic spread, coupled with a phylodynamic model of the within-host pathogen evolution. It is validated with a case study, modelling a rapid punctuated evolution of SARS-CoV-2, based on global and contemporary genomic surveillance data, during the COVID-19 transmission within a large heterogeneous population. We demonstrate that the model captures the essential features of the COVID-19 pandemic and the novel coronavirus evolution, while retaining computational tractability and scalability.

Keywords agent-based model, phylodynamics, punctuated evolution, pandemic, complexity

*: *These authors contributed equally*

1 Main

Digital epidemiology is an emerging field, rapidly capitalising on the increasing availability of high-resolution genomic, immuno-epidemiological, demographic and human mobility data, social media analytics, high-performance computing power, as well as innovations in simulation methods and data science. In principle, these diverse sources of data should allow modellers to develop informative multi-scale pandemic models with substantially higher accuracy and predictability. Yet, pandemic modelling continues to face significant challenges due to (i) the inherent complexity

of rapidly evolving pathogens, (ii) population heterogeneity (demographic, immunological and behavioural), (iii) multi-objective public health interventions carried out under severe pressure and non-trivial social dynamics.

The modelling complexity is exacerbated by (iv) different time scales needed to model pandemics on multiple levels, ranging from within-host changes in implicated pathogens, to natural infections in individuals and their social behaviour and interactions (v) fragmentation of data across heterogeneous sources, and (vi) computational complexity of multiple simulations over a sufficiently long horizon, required to establish statistically significant outcomes. Multi-scale models often suffer from the “curse of dimensionality”, when computational costs increase exponentially with the number of degrees of freedom [1].

A principal modelling problem is the presence of feedback loops: for example, pandemic mitigation measures may put an evolutionary pressure on the pathogen, causing the emergence of more transmissible lineages. Higher transmissibility may increase the need for more vigorous interventions, which in turn may cause changes in how populations respond and behave, and increase evolutionary pressure on the pathogen. One possible outcome of this feedback loop is the establishment of recurrent waves and a nonlinear transition from emerging to endemic pathogen. Consequently, multi-scale modelling of a major pandemic crisis, such as the COVID-19, quickly becomes intractable.

Over the last decades, stochastic agent-based modelling (ABM) has been established as a robust tool for tracing fine-grained effects of complex intervention policies in diverse epidemic and pandemic settings [2, 3, 4, 5]. Most recently, these studies produced policy recommendations developed for COVID-19 control, and adopted in Australia [6, 7, 8], the USA [9], the UK [10], and broadly by the WHO [11]. A largely unexplored avenue to leverage the precision and fidelity of ABMs is to extend them with comprehensive phylodynamic modelling of evolving pathogens, going beyond existing phylogenetic models which define simplified evolutionary landscapes [12, 13]. This necessitates a new class of multi-scale phylodynamic ABMs.

An optimal framework for multi-scale phylodynamic agent-based modelling should include several distinct capabilities that produce quantifiable outcomes. These include the ability to:

1. Model and examine epidemic or pandemic patterns over a mid- to long-term timeframe, with respect to complex transmission and immunological profiles, affected by varying pharmaceutical and non-pharmaceutical interventions:
 - (a) Reproduce and predict salient peaks and recurrent waves of incidence, prevalence, and other epidemic dynamics.
 - (b) Explore possible transitions and pathways to endemicity or elimination.
2. Examine the pathogen fitness with respect to its phylodynamics:
 - (a) Trace changes in transmissibility with respect to pathogen mutations. This includes analysis of the average basic reproductive ratio (R_0) within the population, and the accumulated mutations measured by the average genomic distance between a circulating genome and the ancestral genome, i.e., in terms of the substitution rate (the number of non-synonymous mutations per year observed in detected cases).
 - (b) Examine the genomic structure-function dynamics. This analysis quantifies the individual contributions of amino acids to changes in the pathogen’s fitness, and traces the dynamics of these contributions over time.
3. Detect and evaluate the emergence and dominance of variants of concern:
 - (a) Explore temporal alignments between phylodynamics and disease dynamics, e.g., relating accumulated mutations, genomic diversity, and saltations in pathogen fitness to incidence peaks.
 - (b) Detect abrupt changes in genomic diversity, and evaluate emergence of variants of concern, by using appropriate quantitative techniques (such as Augmented Dickey-Fuller stationarity test, CUSUM, etc.), supported by suitable data visualisation methods (such as phylogenetic trees).

A robust phylodynamic ABM needs to be validated by comparing its target outcomes against the ground truth dynamics. Once validated, it can be used to explore diverse counter-factual scenarios with respect to phylodynamic, demographic and immuno-epidemiological characteristics. We illustrate the ground truth dynamics, matching the three capabilities, in Figures 1 to 4, by using available genomic and disease surveillance data on COVID-19 and SARS-CoV-2 from 2020 to 2024.

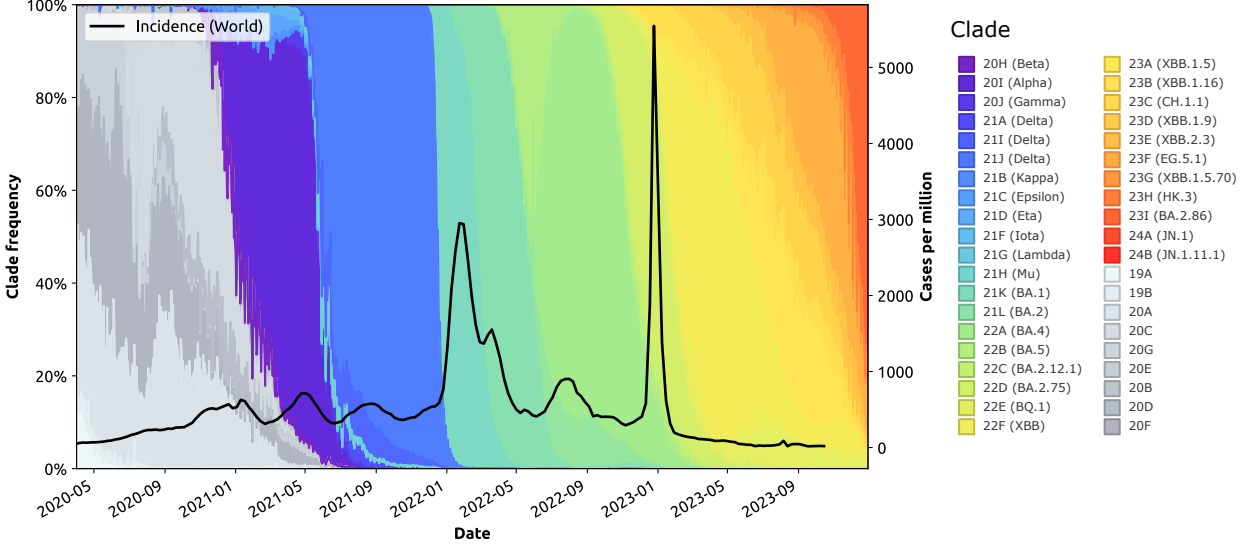


Figure 1: Capability 1. Pandemic patterns in terms of the worldwide incidence (solid, black line), measured as new weekly cases per million [14], overlaid with the frequency of circulating variants between 2020 and 2024, plotted using open SARS-CoV-2 sequence data (7,075,645 samples) from GenBank and the Robert Koch Institute, processed by Nextstrain [15].

To demonstrate **Capability 1**, a modelling framework is expected to generate pandemic or epidemic patterns aligned with ground truth (i.e., observed data). For example, Fig. 1 shows patterns observed in global data reported during the COVID-19 pandemic, highlighting prominent peaks and recurrent incidence waves. We point out that each incidence peak is temporally aligned with the emergence of a new variant of concern. Notably, the two most prominent incidence peaks occurred in early 2022 and early 2023, corresponding to the dominance of Omicron BA.1 and Omicron XBB, respectively. These observations suggest a complex interplay between pandemic patterns and evolutionary phylodynamic features of the viral variants in circulation.

Capability 2 demands a dynamic analysis of the pathogen fitness in terms of observable phylodynamic characteristics. For example, Fig. 2 relates the growing transmissibility of SARS-CoV-2 to (i) the mutations accumulated relative to its ancestral strain, and (ii) the associated genomic diversity of the evolved pathogen. It also places the fitness dynamics in the context of the genomics.

Specifically, Fig. 2 (A) shows a rapid punctuated increase in fitness, with two significant surges in the relative transmissibility (measured relative to the basic reproductive ratio of the ancestral strain R_A), and the accumulated mutations, observed during early 2021 and early 2022. The accumulated mutations continued to grow after 2022, reaching 130 substitutions by mid-2024 at the rate of roughly 30 substitutions per year, according to linear regression (Fig. 2 (B)).

Furthermore, notable changes in the amino acid presence were observed across the genome, particularly the spike region, between the start of the pandemic and late 2023, as illustrated for the 5' end of the S gene in Fig. 2 (C–D). These shifts occurred preferentially at specific positions, deviating significantly from the ancestral genome, and thus, potentially contributing to the increase in fitness.

Capability 3 is focused on the emergence and dominance of variants of concern, in the context of phylodynamic and epidemiological dynamics. For example, Fig. 3 (A) traces a continuous increase in the accumulated mutations which is contrasted with the fluctuating genomic diversity. Unlike the mutations \hat{D} which accumulated relative to the ancestral strain, the genomic diversity, measured as the pairwise distance \bar{D} among the genomes of co-circulating pathogens, shows only a marginal increase during the observed period. We extracted phylodynamic features using the data recorded until early 2024, noting a significant drop in the number of sequenced samples worldwide from 2024

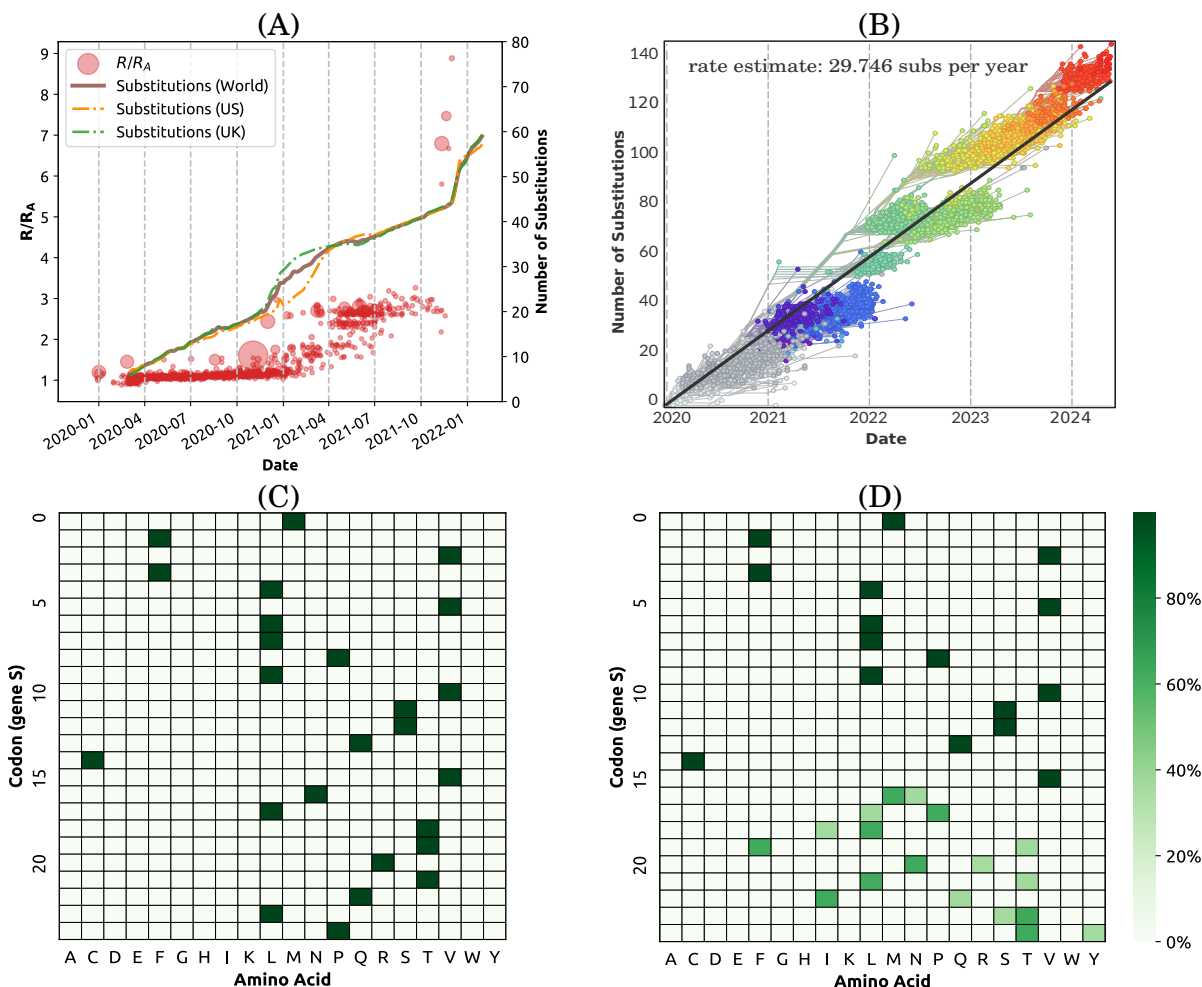


Figure 2: Capability 2. Pathogen fitness with respect to its phylodynamics. (A) Punctuated growth of fitness, measured relative to the basic reproductive ratio of the ancestral strain R_A [16] (represented as the R/R_A , red circles), overlaid with the average accumulated mutations across the population (represented by the Hamming distance \hat{D}), also measured relative to the ancestral strain. (B) Accumulated mutations \hat{D} , expressed as the number of substitutions relative to the ancestral genome. The black line shows the linear regression of the accumulated mutations (\hat{D}) between 2020 and 2024, with a gradient of roughly 30 substitutions per year. We refer to Fig. 1 for clade colours. For visualisation purposes, we show around 4,000 genomes [17]. (C, D) Histograms of amino acids over the first 26 codons in gene S of the COVID-19 ancestral strain (C), and 631 randomly selected genomes from GenBank and the Robert Koch Institute between 17 and 31 December 2023 (D) [15].

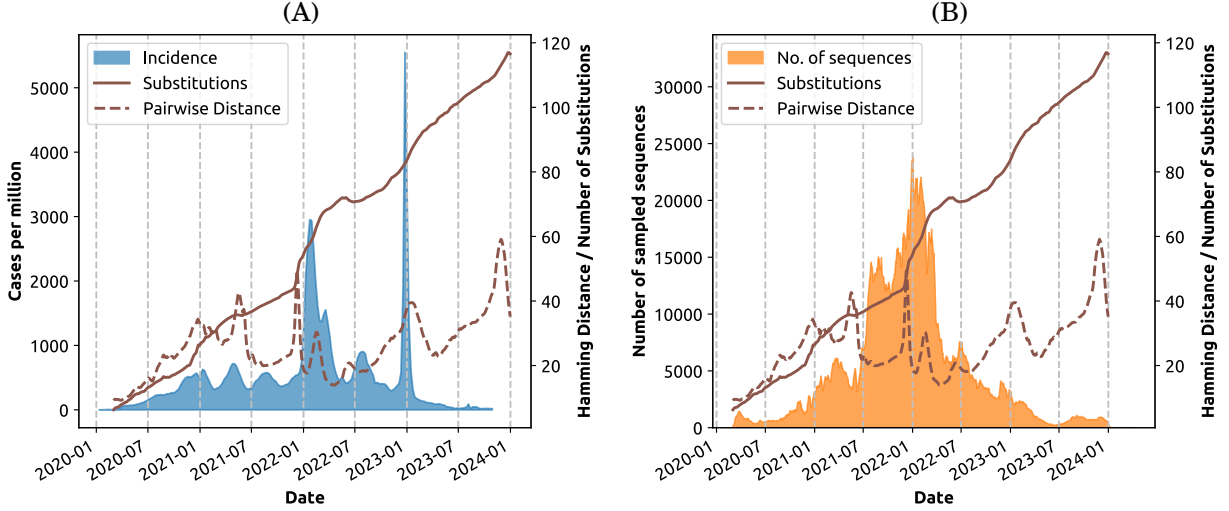


Figure 3: Capability 3 (i). Temporal alignments between phylodynamics and disease dynamics. (A) The global COVID-19 incidence (cases per million, shaded blue area) overlaid with accumulated mutations \hat{D} (solid brown line) and genomic diversity \bar{D} (represented by the average pairwise distance between two randomly selected genome sequences, dashed brown line). (B) The number of sequences, measured using a 7-day moving average, captured by the open SARS-CoV-2 sequence database processed by Nextstrain [15] (shaded orange area) overlaid with accumulated mutations \hat{D} across the genome (solid brown line), and genomic diversity \bar{D} (dashed brown line).

onwards (Fig. 3 (B)).

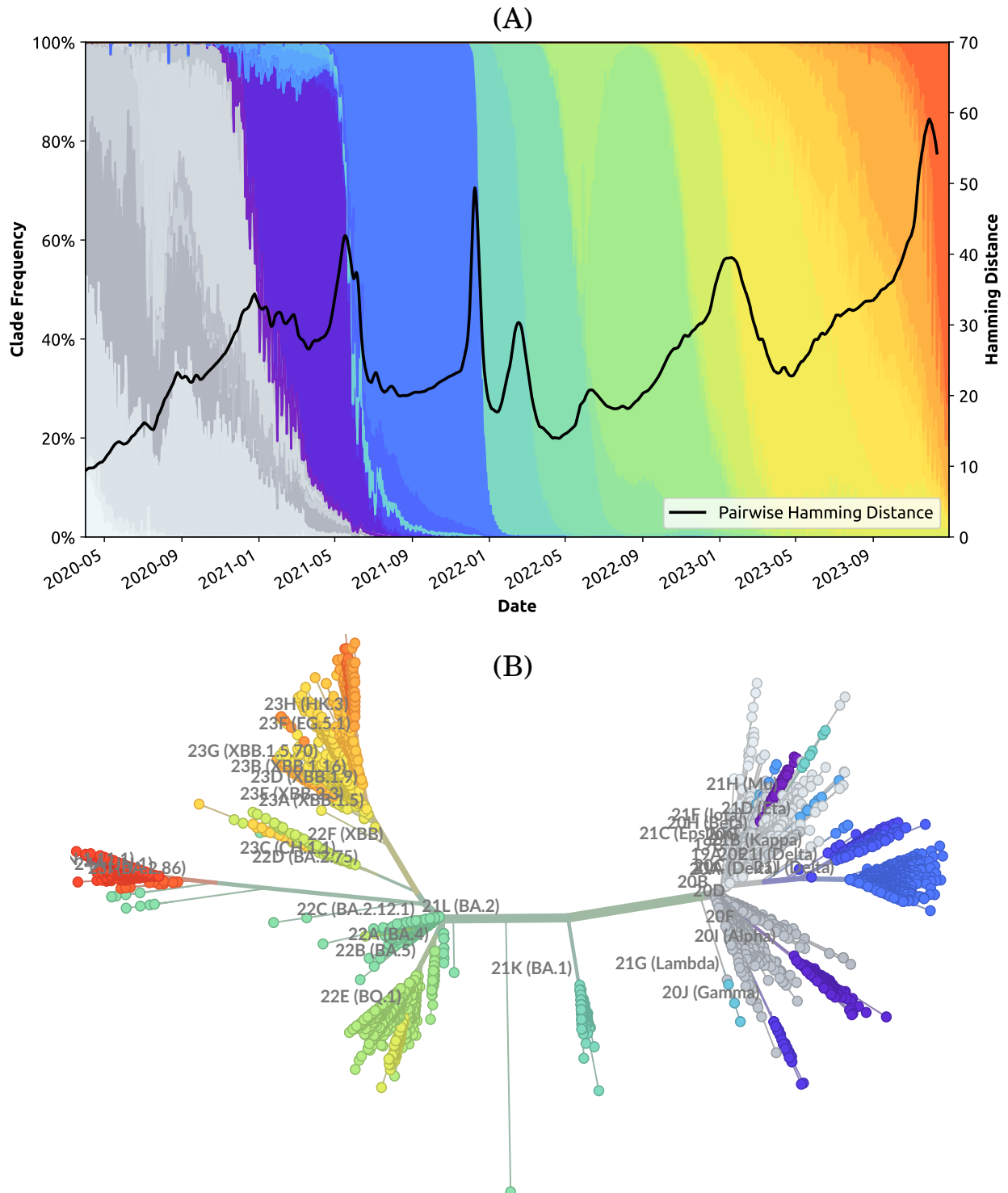
In general, abrupt changes in genomic diversity are related to the frequency of different variants reported during the pandemic period (Fig. 4 (A)), and considered in context of the corresponding phylogenetic tree (Fig. 4 (B)). For example, we observed that during the rapid evolution of SARS-CoV-2, sudden decreases in circulating diversity correspond to specific lineages becoming dominant, whereas new variants are more likely to emerge during periods of increasing circulating diversity (i.e., increasing pairwise genomic distance). Importantly, the observed changes in the pairwise distance are also reflected in the phylogenetic tree produced from representative sub-sampling of global sequences (Fig. 4 (B)). Branches corresponding to new variants of concern tend to descend from more basal lineages than the main lineages circulating immediately prior to their emergence. These evolutionary saltations may explain step changes in transmissibility and virulence.

2 Results

We present an agent-based modelling (ABM) framework for computational modelling of pathogen phylodynamics, focusing on communicable diseases within heterogeneous populations. The key component is PHASE TRACE, **Phylodynamic Agent-based Simulator of Epidemic Transmission, Control, and Evolution**, a versatile multi-scale simulator for modelling rapid pathogen evolution. The framework also includes several phylodynamic measures aimed to identify the emergence of novel pathogen variants.

PHASE TRACE was developed upon several existing large-scale pandemic simulators, including the Australian Census-based Epidemic Model (ACEMod) of pandemic influenza [18, 19, 20], and the Agent-based Model of Transmission and Control of the COVID-19 pandemic in Australia (AMTraC-19) [6, 21]. These ABMs have been successfully validated and used in simulating multiple waves of influenza [18] and COVID-19 [6, 5, 22, 23, 24], mitigated by various interventions, including mass-vaccination roll-outs and non-pharmaceutical interventions.

Similar to these models, PHASE TRACE simulates the disease transmission in discrete time in an artificially generated population with census-based demographic characteristics and commuting patterns [25]. Going beyond the existing models, PHASE TRACE is capable of simulating the inter-host transmission of multiple pathogen variants within a



heterogeneous population, the within-host evolution of pathogens, and immuno-epidemiological feedback.

In this section, we overview the model’s multi-scale approach (subsection 2.1). We then apply PHASE TRACE to a case study of SARS-CoV-2, and evaluate the simulated phylodynamics against the modelling capabilities and objectives (subsection 2.2). Finally, we explore counterfactual scenarios by varying specific assumptions of the case study, e.g., the role of chronic infections and population sizes (Supplementary section F).

2.1 Model overview

Distinct from many computational models that focus solely on epidemiological dynamics within host populations or evolutionary dynamics within pathogen populations, PHASE TRACE simulates dynamic feedback across three scales: (i) micro-scale: within-host evolution and the evolutionary landscape of circulating variants; (ii) meso-scale: agent-to-agent interactions and inter-host transmission; and (iii) macro-scale: public health interventions (i.e., non-pharmaceutical interventions and vaccination) at the population level.

This multi-scale feedback is realised by incorporating four concurrent dynamics implemented in distinct processing layers: demographic, epidemic, immunological, and phylogenetic, as illustrated in Fig. 5. The demographic layer defines the population structure (i.e., host type) and social groups constraining agent interactions. The transmission is simulated by the epidemic layer, tracing individual interactions occurring within and across different social contexts, including residential (e.g., household) and professional settings (e.g., working group). In addition, the epidemic layer sets out an intervention scenario, with varying NPI adoption levels and vaccination strategies, thus reflecting changes in health policy and public opinion [26, 27]. The infection transmission depends on the agents’ immunity levels derived from their individual dynamic history of exposures and immunisation, determined by the immunological layer. There are two infected host categories: typical infected hosts and chronically infected hosts, with the latter representing hosts with *persistent SARS-CoV-2 infections* arising due to some underlying factors and resulting in longer recovery periods [52, 46] (see Supplementary section A.4). The phylogenetic layer determines the within-host evolution of pathogens in terms of mutation and selective pressure. Section 4 provides a detailed description and implementation of these four layers.

2.2 Case study: Rapid punctuated evolution of SARS-CoV-2

PHASE TRACE was calibrated to the COVID-19 pandemic and the evolutionary trajectory of SARS-CoV-2 over the period of four years, from 2020 to 2023. The results comprise simulations over a six-year period (2020 — 2025), across three artificial agent populations: 1.7 million agents (small), 8 million agents (medium), and 25.4 million agents (large), as described in Supplementary Section B.

In calibrating PHASE TRACE, we examined COVID-19 pandemic and the size of susceptible, recovered and vaccinated populations (Capability 1); phylodynamic characteristics including transmissibility, fitness, the number of accumulated mutations relative to the ancestral strain, and genomic diversity (Capability 2); and the emergence of variants, analysed using the phylogenetic tree and statistical methods (Capability 3). The robustness of the model is established through sensitivity analysis, by varying key parameters and assessing their impact on simulation outcomes. See Supplementary Table 4 for the list of phylogenetic parameters used in the SARS-CoV-2 case study and Section G for more information on sensitivity analysis.

Capability 1. Our results show recurrent incidence waves as illustrated in Fig. 6 (A), in concordance with empirical observations (Fig. 1). Although the first simulated incidence peak (detected during 2021) is noticeably higher in larger populations, the incidence converged to around 2,000 cases per million after 2023, indicating endemicity in all simulated populations.

The main contributing factor to the recurrent incidence is the fluctuating number of recovered individuals (Fig. 6 (B)) that replenish the susceptible population after their immunity wanes. This subsequently leads to an increasing number of re-infection cases. Additionally, due to the diminishing immunity, declining vaccine uptake, and declining adoption of social distancing in the population (simulated to be decreasing from 50% of hosts in 2020 to 20%

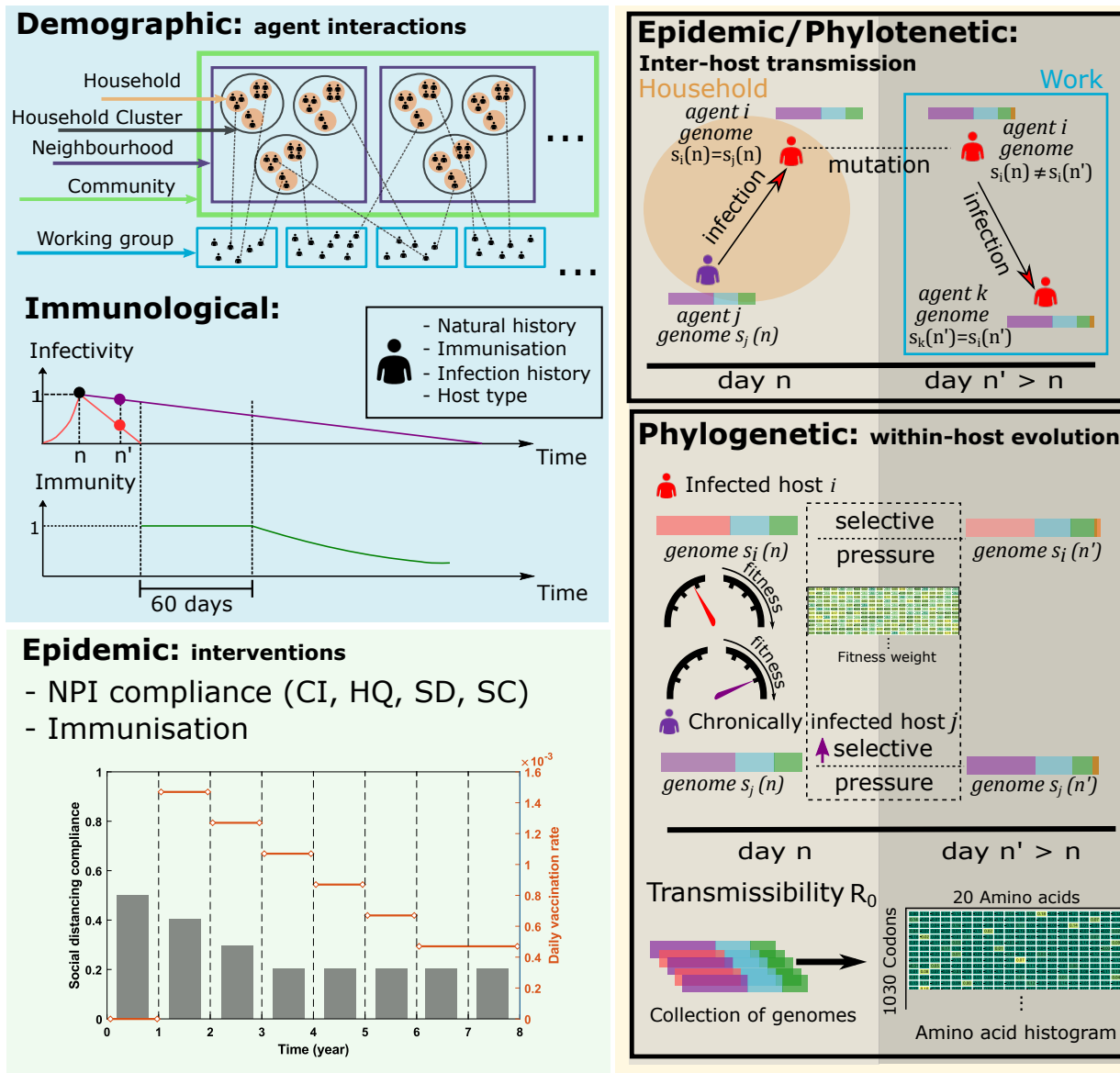


Figure 5: Model overview. The demographic layer assigns agents to social contexts, including household, household cluster, neighbourhood, community, and working group/school. The immunological layer keeps track of the agents' immunisation records, infection histories, and the host types. The epidemic layer describes an intervention scenario, in terms of NPIs and their adoption levels: case isolation (CI), home quarantine (HQ), social distancing (SD), and school closure (SC), along with a dynamic immunisation schedule. Both epidemic and phylogenetic layers affect inter-host transmission (e.g., on day n , a chronically infected host j infects their family member i and passes genome $s_j(n)$ to agent i). The phylogenetic layer determines the genomic mutations under various strengths of selective pressure, and traces changes in transmissibility (reflected in R_0). The fitness of each genome is determined by a weight table, quantifying the contributions of each amino acid in a given codon position.

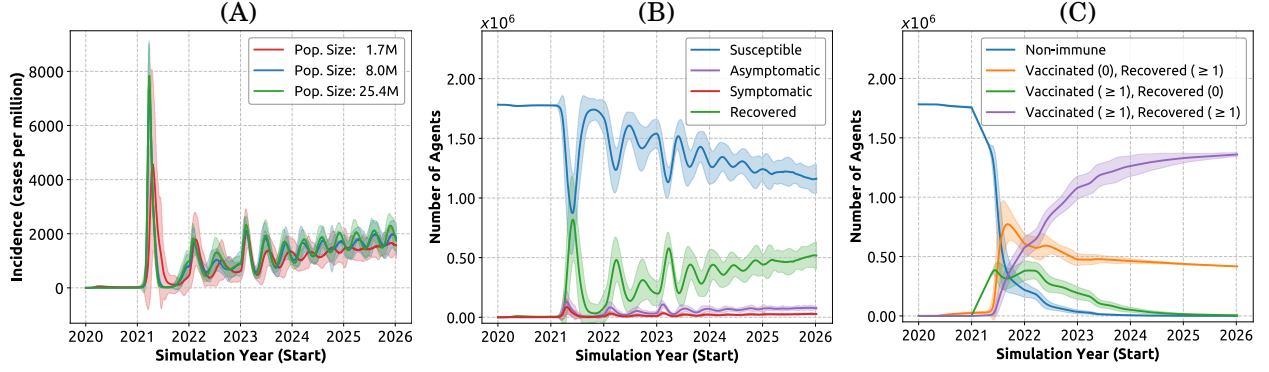


Figure 6: Simulated pandemic patterns (Capability 1) shown as mean (solid line) and standard deviation (shaded area). (A) Detected incidence simulated in population sets of 1.7 million (red), 8 million (blue), and 25.4 million (green). (B) Population in different health states, including susceptible (blue), asymptotically infected (purple), symptomatically infected (red), and recovered (green). (C) Population with different immunisation and infection history. Numbers in brackets denote the number of vaccination or infection records. Individuals with multiple vaccinations or infections (more than 2) are grouped together for simplicity. (B) and (C) are generated using the population set of 1.7 million. Mean and standard deviation were obtained from approximately 30-50 realisations.

from 2024 onwards), the overall incidence slightly increases over the simulated timeframe after the first peak (Fig. 6 (A)).

We also observe an increasing number of individuals with multiple vaccination and infection records (Fig. 6 (C)). These dynamics slow down the transmission but are unable to completely eliminate the spread, due to the waning immunity and reduced vaccine efficacy against mutated variants. Figures 6 (B) and (C) only show dynamics for the 1.7 million population. We note that the pandemic patterns are consistent across different population sizes, as shown in Supplementary Fig. 19.

Capability 2. Here we investigate how the pathogen fitness changes during the simulation, given the selective pressure on circulating strains which “compete” in terms of their transmissibility. We begin by exploring how the phylodynamic characteristics, such as accumulated mutations, develop along the observed increase in simulated fitness (Capability 2 (i)).

Importantly, we observe a concurrent punctuated increase (i.e., ‘jump’) in both transmissibility R_0 , i.e., fitness K (Fig. 7 (A)), and accumulated mutations \hat{D} (Fig. 7 (B)) at the start of 2021. This is a pattern which is also observed in empirical data illustrated in Fig. 2 (A). The timing of the simulated ‘jump’ aligns well with the first incidence peak in 2021, illustrated in Fig. 6 (A). This alignment can be explained by the accumulation of fitness-increasing mutations in chronically infected hosts, due to a higher selective pressure on pathogens evolving in these hosts; consequently generating a highly transmissible strain (i.e., a variant of concern) (see Supplementary Section A.4). This is confirmed by a comparison with a counterfactual scenario without chronically infected hosts in which the jump is not observed, as shown in Fig. 26 and analysed in Supplementary Section F.

Similar jumps are observed at later pandemic stages in a majority of individual simulation runs (see Fig. 7 (C) and Supplementary Figures 20 to 22), but their timing differs across realisations, and so the average profiles shown in Fig. 7 (A) and (B) smooth the saltations. The very first saltation is mostly aligned across the individual realisations, and so it is quite prominent in both K and \hat{D} . Figure 7 (C) shows that the fitness K and accumulated mutations \hat{D} are strongly temporally aligned (with Pearson correlation 0.99 over 2, 191 data points), suggesting that saltations in transmissibility are produced by accumulated mutations.

We also observe that the fitness and accumulated mutations are slightly higher with increasing the population size, although these changes are much smaller than the population differences. All three population sets produced saltations in fitness and accumulated mutations. However, in smaller populations (i.e., 1.7 million), profiles of these two measures are not only slightly lower but also somewhat less abrupt, relative to the profiles produced in larger populations (8

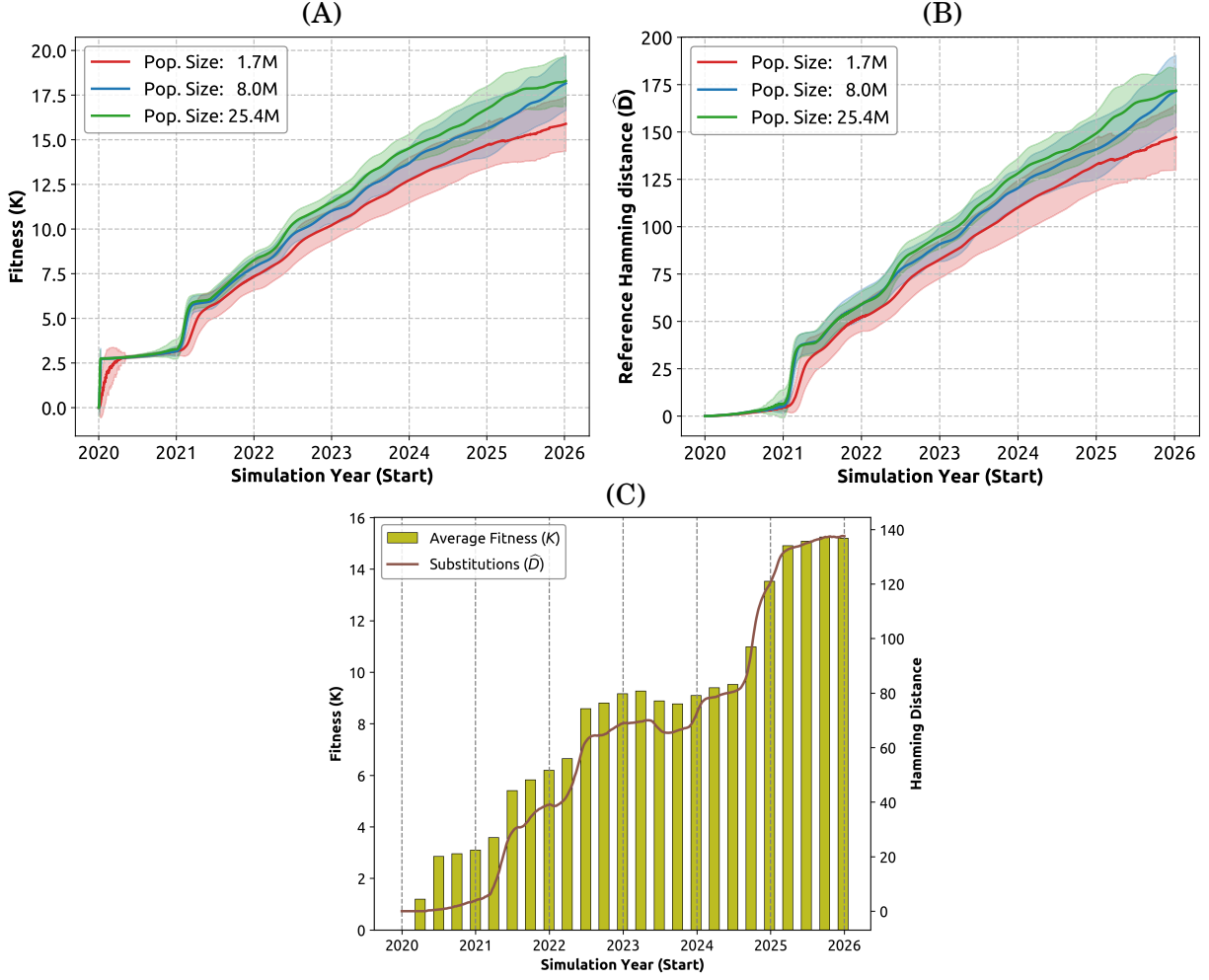


Figure 7: Simulated phylodynamic measures (Capability 2(i)), shown as mean (solid line) and standard deviation (shaded area) for different populations: 1.7 million (red), 8 million (blue), and 25.4 million (green). (A) Growing pathogen transmissibility, interpreted as fitness K . (B) Accumulated mutations \hat{D} , measured at each time point by the average reference Hamming distance between the circulating variants and the reference (ancestral) variant. The mean and average were obtained from approximately 30-50 realisations. (C) Single realisation, showing alignment of the average transmissibility, i.e., fitness (K , olive bars), and the accumulated mutations (\hat{D} , solid brown line).

million and 25.4 million).

To explain the punctuated increase in fitness, we traced changes in the distribution of fitness contributions across the simulated genome (Capability 2(ii)) by comparing the relative frequencies of amino acids in simulated ancestral genome (Fig. 8 (I)) and the evolved distributions in circulating genomes after six simulation years (Fig. 8 (II)). In simulated dynamics, we observed a clear shift towards amino acids with positive fitness contributions, in accordance with empirical observations (Fig. 2 (E) and (F)). This observation indicates that the viral mutations are subject to selective pressure transitioning to a higher point in the viral fitness landscape. Section 4 and Supplementary section A.3 provide a detailed description of the fitness contribution method.

Capability 3. In pursuing our final objective, we explore the emergence and dominance of variants of concern in the simulated dynamics. We begin by examining whether the simulated phylodynamic characteristics are temporally aligned with the disease incidence. We note that saltations in the accumulated mutations \hat{D} can be matched by peaks in the genomic diversity \bar{D} , as shown by Fig. 9. These diversity peaks indicate a rise of a new variant (i.e., increase in

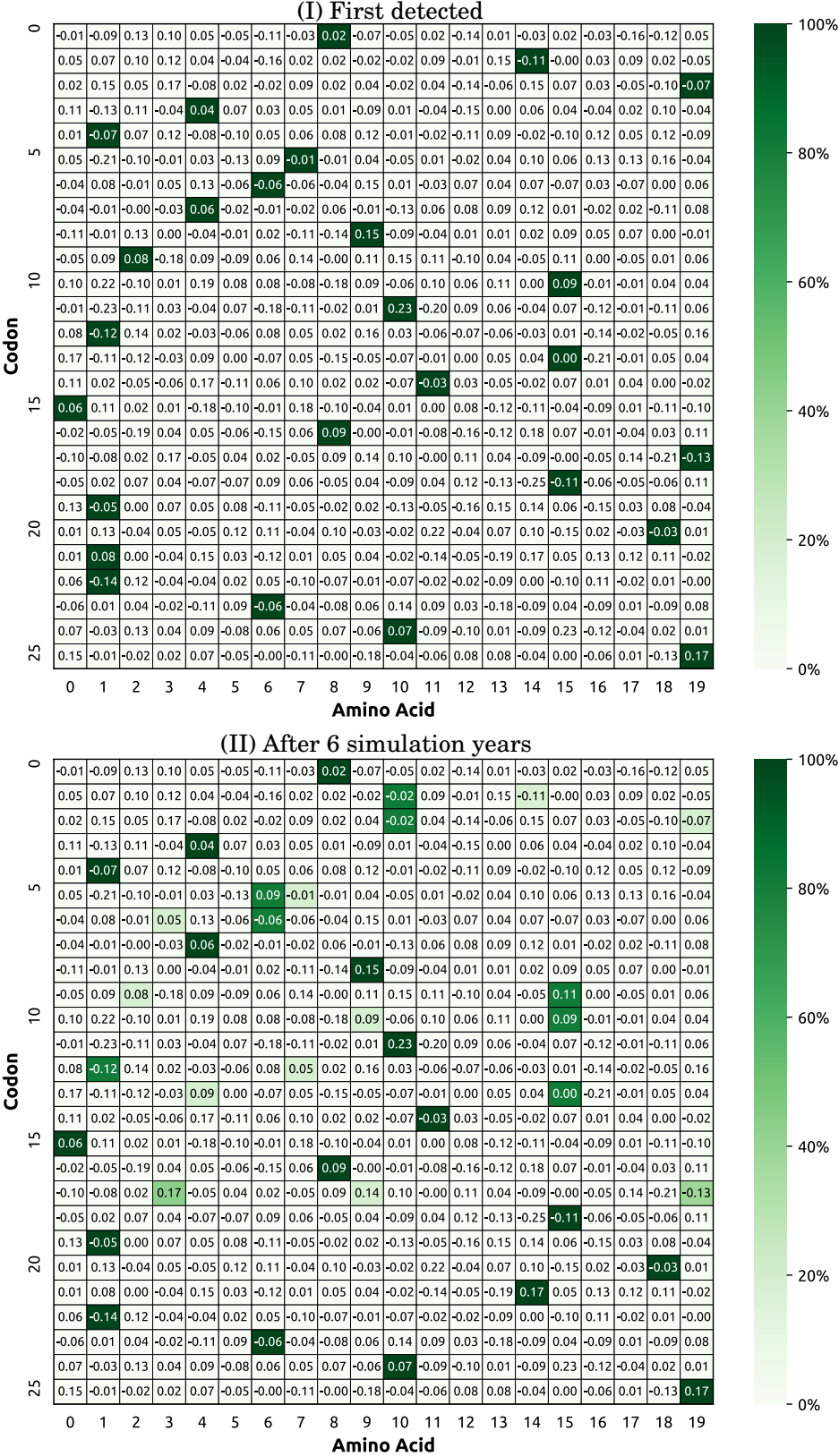


Figure 8: Snapshots of amino acids – codons histograms at different simulation time steps, obtained from a single realisation using the population of 1.7 million agents (Capability 2(ii)). Amino acids in the first 26 codons (i.e., the first 78 nucleotides) are shown here for simplicity. Note that the numerical fitness contributions are generated following distributions specified in Supplementary section A.3 prior to each simulation run. (I) The histogram produced for the first day when cases were detected, and (II) the evolved histogram computed from 500 randomly selected genomes after 6 simulation years. The colour intensity represents the frequency of a given amino acid–codon combination in the sampled genome(s). The value shown in each histogram cell represents the pre-defined amino acid contribution to fitness.

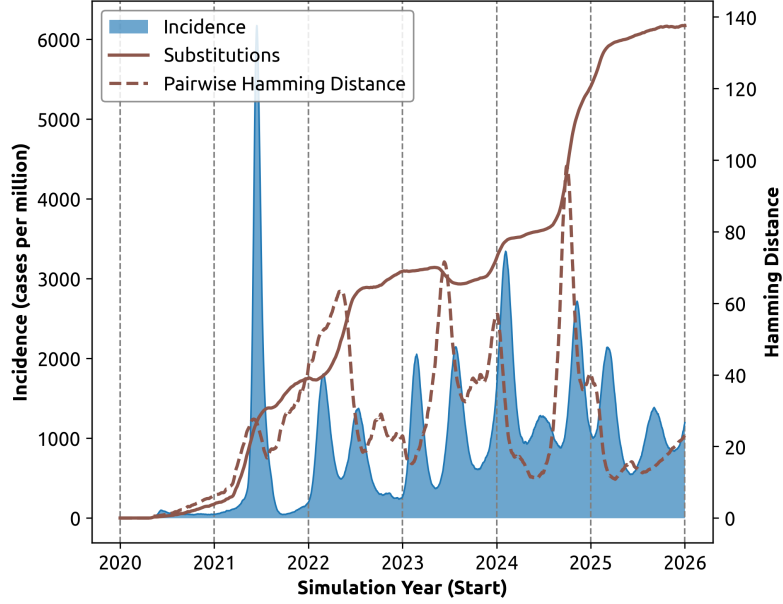


Figure 9: Temporal alignment of phylodynamics and epidemiological dynamics (Capability 3i), simulated for a 1.7 million population over a 6-year period. Alignment of epidemic incidence (shaded blue area), accumulated mutations (\hat{D} , solid brown line), and genomic diversity (\bar{D} , dashed brown line). Profiles are shown for a single realisation.

diversity), followed by its dominance (i.e., decrease in diversity) until yet another variant emerges. In turn, these abrupt changes correspond to incidence peaks, that is, there is a notable synchrony between dynamics of the incidence and the genomic diversity \bar{D} . At the same time, not all incidence peaks can be explained by the changes in genomic diversity or the saltations in fitness.

These observations are well aligned with the empirical data for the first four COVID-19 pandemic years. In particular, Fig. 3 (A) suggests that, while the accumulated mutations monotonically increase, the genomic diversity fluctuates along a volatile pattern with periods of drift (i.e., steady increase) followed by rapid increases and sudden collapses in the pairwise Hamming distance. Our simulation produced a similar alignment between the growing accumulated mutations \hat{D} and the fluctuating genomic diversity \bar{D} , as illustrated by Fig. 9. We note that Fig. 9 illustrates the genomic diversity dynamics based on one simulation realisation (for 1.7 million agents). Supplementary Figures 23 to 25 show simulation results across multiple realisations and different population sizes.

Aiming to demonstrate Capability 3 (ii), we quantified the emergence and dominance of variants by analysing the genomic diversity dynamics with a statistical technique based on deviations from Cumulative Sum (CUSUM), and visualising the phylogenetic tree (see Section 4). The analysis was applied to both empirical and simulated data. For empirical data, we detected six notable deviations (Fig. 10 (A)), identifying six emergent and dominant variants between 2020 and 2024. For the simulated data, five deviations were detected between 2020 and 2026 (Fig. 10 (B)).

By aligning the genomic diversity with the incidence dynamics (Fig. 11 (B)), we observe that transitions between the variants which emerged during simulation follow distinct changes in the genomic diversity. We also note stationarity of the genomic diversity, although the time series become less stationary in larger populations (see Supplementary section F.2).

Finally, we constructed a phylogenetic tree using simulation results. The tree is shown in Fig. 11 (A), with the branches colour-coded by the variants identified using CUSUM, corresponding to Fig. 10 (B). Notably, the phylogenetic tree reveals that (1) the new variants emerge at a distance from the ancestral strain, while branching away from more basal lineages, and (2) the variants detected in later years are closer to each other. These observations are consistent with the

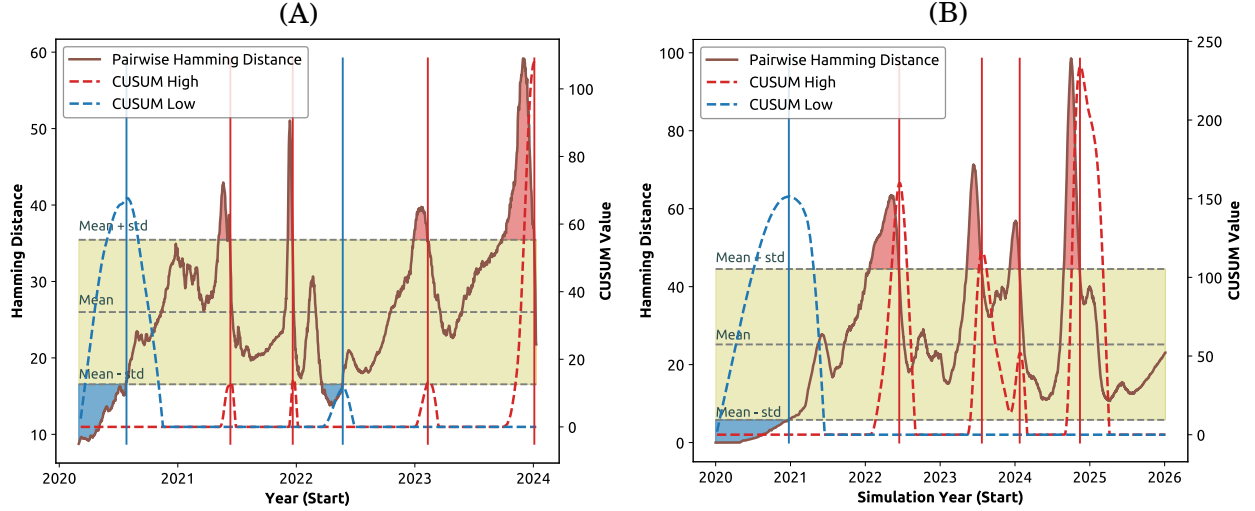


Figure 10: Detection of emerging variants (Capability 3 ii) by applying CUSUM to the genomic diversity quantified by pairwise Hamming distance (\bar{D}). (A) The empirical genomic diversity based on Nextstrain datasets [15]. (B) Simulated genomic diversity in a population of 1.7 million. Vertical lines represent variants detected using CUSUM high (red) and CUSUM low (blue). The yellow shaded area shows the control range around the mean \bar{D} within one standard deviation. Simulated profile in (B) is shown for a single realisation.

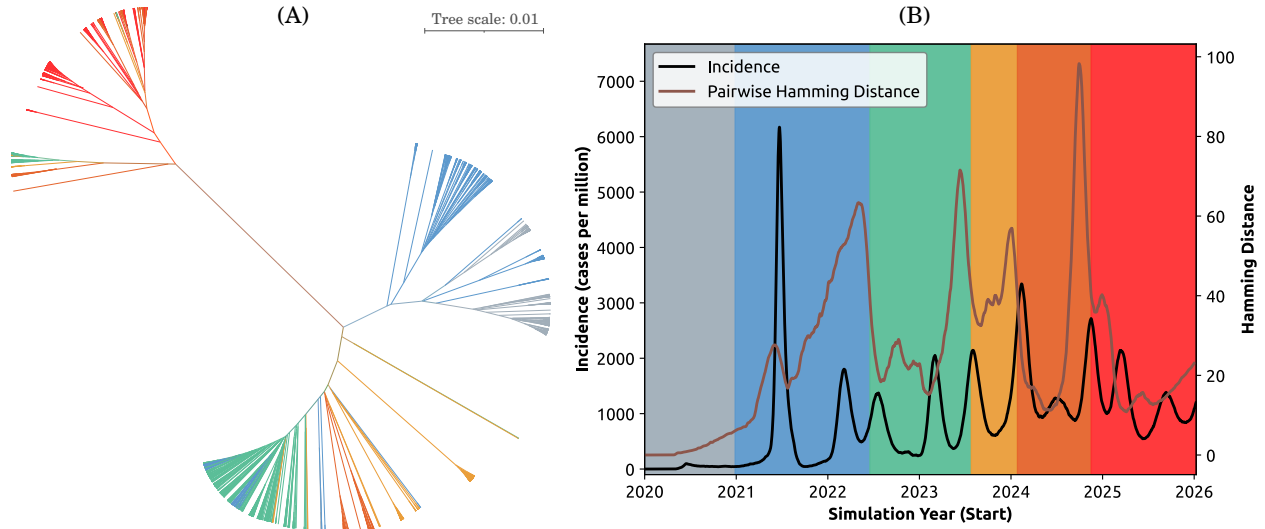


Figure 11: Evaluation of the emergence and dominance of variants (Capability 3 ii). (A) Phylogenetic tree constructed using BEAST [28, 29] and iTol [30], depicting the genomes of the most transmissible strains sampled every half-day. A total number of 4,394 genomes are plotted. (B) Alignment of simulated incidence (solid black line), the genomic diversity (\bar{D} , solid brown line), and the detected variants identified in Fig. 10 (B). Both (A) and (B) are colour-coded according to the day ranges determined by the CUSUM peak detection in Fig. 10.

branching of the phylogenetic tree constructed using empirical data (Fig. 4 (B)).

Overall, these simulation results, aligned with the empirical observations, imply that a rapid punctuated evolution with prominent saltations in transmissibility is driven by accumulation of fitness-increasing mutations relative to the ancestral strain, aided by persistent, chronic infections. The simulated phylodynamics produces a fluctuating genomic diversity, associated with the emergence and dominance of variants of concern, at least during a mid-term pathogen evolution.

3 Discussion

In this study, we identified key requirements for a new class of multi-scale pandemic models. The three considered dynamics included: (1) pathogen evolution, punctuated by the emergence of new pathogen variants, (2) human interactions within heterogeneous populations, and (3) public health interventions aimed at controlling disease transmission. We described specific modelling capabilities, and developed a computational framework, implemented in a comprehensive simulator — PHASE TRACE — which meets these objectives. PHASE TRACE is capable of modelling the spread of infectious diseases while accounting for the evolutionary trajectory of pathogens across diverse demographics. We validated the framework with a COVID-19 case study, by calibrating PHASE TRACE to the phylodynamic and epidemiological characteristics of SARS-CoV-2, and simulating the corresponding immuno-epidemiological and phylodynamic patterns across heterogeneous population settings, scaling the demographics to different sizes. We then applied different phylodynamic measures to analyse the simulated dynamics to detect emerging and dominating pathogen variants, aligning the outcomes with empirical observations. PHASE TRACE can also be calibrated to pandemic scenarios related to other respiratory diseases with known phylodynamic and epidemiological characteristics. However, scenarios related to non-respiratory diseases (e.g., foodborne epidemics, vector-borne diseases) warrants further research.

In particular, PHASE TRACE reproduced recurrent incidence waves with salient initial peaks and a transition to endemicity (Capability 1). These observations showed that, given the waning immunity and reduced vaccine efficacy against emerging variants, the adopted NPIs and vaccination roll-outs would not eliminate the spread completely. Importantly, the simulated phylodynamics produced a rapid punctuated evolution, and this was explained in terms of the accumulation of fitness-increasing mutations within chronically infected hosts. This increase was further confirmed by a clear shift in the simulated distribution of amino acids towards fitness-increasing mutations, appearing due to selective pressure (Capability 2). Finally, we related the emergence and dominance of variants of concern to prominent changes in genomic diversity. This analysis was supported by visualisation of the phylogenetic tree and relevant stationarity tests (Capability 3).

PHASE TRACE is designed to support the testing of different hypotheses by simulating counterfactual modelling scenarios. For example, chronic infections have been hypothesised to contribute to the rapid punctuated evolution of SARS-CoV-2, being often associated with accelerated substitution rates, and a higher genetic diversity and selective pressure [31]. We applied PHASE TRACE to investigate the potential role of chronic infections on the pathogen evolution by comparing resultant phylodynamics with and without chronically infected hosts (see Supplementary section F.1).

Computationally, PHASE TRACE involves a nested stochastic simulation, where the (micro-scale) within-host pathogen evolution is simulated in every artificial agent, while the disease transmission is simulated based on the (meso-scale) agent interactions within a heterogeneous population. Finally, the (macro-scale) public health interventions, such as NPIs and vaccination, are simulated at the population level, constraining the actions of individual agents. The addition of immunological and phylogenetic layers significantly extended the capabilities of PHASE TRACE relative to state-of-the-art pandemic ABMs, although at the cost of higher computational complexity and the need to integrate fragmented data inputs. Nevertheless, the approach retains computational tractability and scalability (see Supplementary Section H).

In our case study, we simplified the phylogenetic model, partitioning it into spike and non-spike regions, with an overlapping region representing epitopes containing genetic information relevant to triggering immune responses (i.e., transmissibility and antigenicity). We also assumed that at any given time, each infected host can only carry a single strain, without exploring the possibility of co-infection (i.e., a simultaneous infection by multiple strains). For computational efficiency, we also reduced the genome length to a tenth of the SARS-CoV-2 genome length. This may partially explain why the genomic diversity becomes less stationary in larger populations. Furthermore, we did not exhaustively explore the impact of different weight tables, defining the fitness contribution of amino-acids, on the genomic diversity over time and its resultant (non-)stationarity. In addition, the employed stationarity test (ADF) is known to be sensitive to the number of included lags in the time series. These limitations may be overcome in future studies, further enhancing the modelling scope and range of applicability of PHASE TRACE.

4 Methods

4.1 Multi-layer architecture of PHASE TRACE

PHASE TRACE is a large-scale stochastic simulator developed to model the mid- to long-term phylodynamics of pathogens within a heterogeneous population of hosts. Computationally, each agent in PHASE TRACE is represented as an object with multiple attributes which can be modified by processing layers: (A) Phylogenetic, (B) Demographic, (C) Epidemic, and (D) Immunological, as illustrated in Fig. 12.

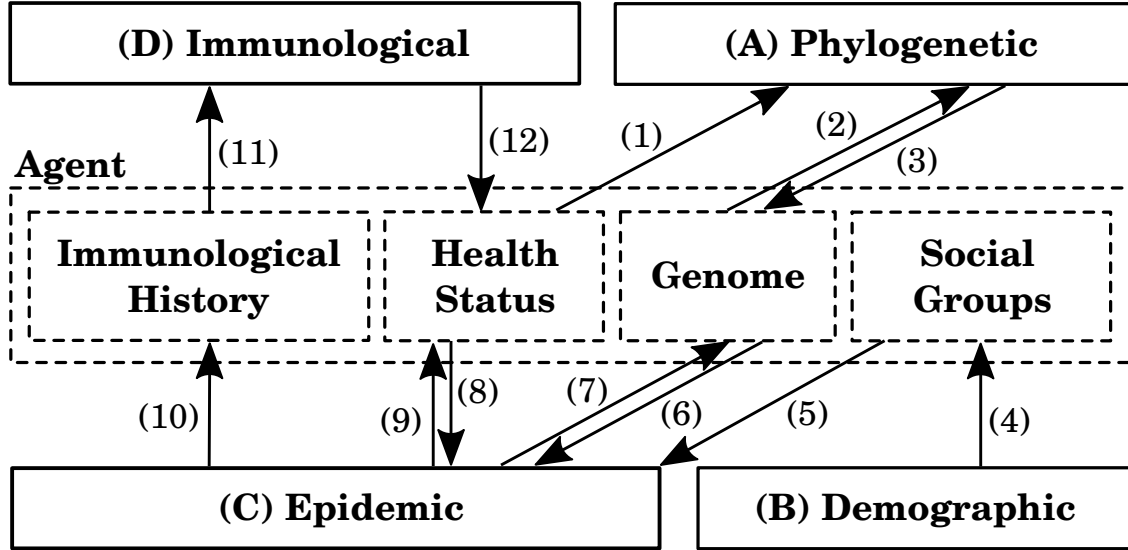


Figure 12: Architecture of PHASE TRACE with four processing layers (A–D) and twelve data flows updating four core attributes of the *Agent* objects.

Each agent has four core attributes: (i) immunological history which records past infections and vaccinations, as well as the associated time stamps of these events; (ii) health status, which tracks the agent’s current health state (Susceptible, Asymptomatically Infectious, Symptomatically Infectious, or Recovered), infected host category (typical infected or chronically infected), and the current immunity against circulating variants; (iii) genome profile of the variant carried by the agent (if infected); and (iv) the social groups, which indicate the social contexts where interactions occur.

The flows between processing layers and agent attributes are directional, as illustrated in Fig. 12: the flows from processing layers to agent attributes modify the attributes, while the flows from agent attributes to processing layers influence the processing layer, as described below.

(A) Phylogenetic: this layer simulates mutations and selective pressure on the genome carried by an infected agent, as detailed in Supplementary Section A. Once the agent becomes infectious, the Phylogenetic layer receives input on the agent’s health status, including the host type category via (1), and the genome profile derived from the infection source via (2). The mutated genome is then saved in the agent’s genome attribute via (3).

(B) Demographic: prior to the simulation, this layer generates a heterogeneous artificial population of a specified size, based on 2021 Australian Census data [32]. The generated demographics are used in constructing the social groups via (4), determining each agent’s social mixing contexts which constrain agent interactions. These contexts include (a) residential contexts, such as households, household clusters, and statistical areas (SAs) at various resolution levels; and (b) studying/workplace environments, such as schools or working groups, depending on the agent’s age group. Details on the Demographic layer and artificial population generation are provided in Supplementary Section B.

(C) Epidemic: this layer models disease transmission and control, detailed in Supplementary Section C.1. The infection transmission is modelled stochastically, being affected by three agent attributes: social groups which constrain interactions between susceptible and infectious agents, via (5); health status which comprises the agent’s health state

and immunity level, given previous immunological events, via (8); and genome profile which provides a representation of the pathogen infecting the agent, via (6). Having simulated a transmission of infection between two agents, the epidemic layer updates three agent attributes: health status, modifying the agent’s health state, via (9); genome profile, by using the representation of the pathogen variant carried by the source of infection, via (7); and immunological history once the infected agent recovers, via (10).

(D) Immunological: this layer reads from an agent’s immunological history of past infections and vaccinations, via (11); and updates the immunity level as part of the agent’s health status, via (12). Supplementary Section D.1 provides a detailed description of the vaccination component. The immunity levels are also affected by a non-linear accumulation over multiple immunity-boosting events (i.e., compound immunity) and the associated waning effects, detailed in Sections 4.2.3 and D.2.

An efficient implementation of this multi-layer architecture requires a resolution of several computational challenges, given the demanding simulation timeframe (over 6 years) and memory-intensive tasks associated with storing evolving agent attributes, particularly in large populations. To address these challenges, we employed multi-threading processing that computes multiple attributes in parallel in each *Agent* object, with the attributes configured independently from each other to achieve concurrency. In doing so, we significantly increased the computational efficiency by reducing both simulation time and associated computational costs. Supplementary Section H details an analysis of the performance, scalability, and computational resources of PHASE TRACE.

4.2 Multi-scale phylodynamic simulation

This section describes processing layers (A), (C) and (D), highlighting their key dynamic relationships. Since the demographic characteristics of agents, including their social groups, are not updated during simulation, there is no dynamic modelling involved in layer (B), and this layer is described in Supplementary Section B.

4.2.1 Phylogenetic layer (A)

The phylogenetic layer models the within-host evolution (mutation and selection), using pathogen genomes associated with each infected agent, and computes the fitness of circulating variants. An artificial genome contains 3,090 nucleotides (or 1,030 codons) which are associated with 20 known types of amino acids. The genome structure is partitioned into the spike region (100 codons) and the non-spike region (930 codons), with an overlapping region accounting for epitopes (75 codons, with 45 of these located in the spike region and 30 in the non-spike region). Supplementary Section A.1 provides a detailed description of the genome structure, followed by Supplementary Section A.2 describing point mutations.

The pathogen fitness is defined in terms of its transmissibility, reflected in the corresponding basic reproductive number (R_0). To quantify the individual fitness contributions of amino acids at each codon position, we employ a weight table, specifying weights $a_{i,j}$ of $N_A = 20$ types of amino acids across $N = 1,030$ codon positions, as detailed in Supplementary Section A.3. The overall fitness K of a strain with genome s is determined as the sum of these individual contributions:

$$K(s) = \sum_{i=0}^{N-1} a_{i,s(i)} \quad (1)$$

where $a_{i,s(i)}$ is the fitness contribution of amino acid $j = s(i)$ located at codon position i , with $j \in [0, N_A - 1]$.

To re-iterate, the phylogenetic model distinguishes between two infected host categories: typical infected hosts and chronically infected hosts (Supplementary Section A.4). Consequently, there are different selective pressures driving the within-host evolution of pathogens in these categories (Supplementary Section A.5).

We distinguish between mutation and substitution rates. While the mutation rate refers to the frequency of new mutations arising in a genome per unit of time, the substitution rate is the rate at which these new mutations are retained over time within the population [33, 34, 31]. In our case study, the mutation rate is a key input parameter, whereas the average substitution rate emerges as a simulation outcome. We use the attained substitution rate to calibrate the model, by matching the regression coefficient observed in empirical observations, illustrated in Fig. 2 (B).

4.2.2 Epidemic layer (C)

At the start of simulation, pathogens with the ancestral genome are “seeded” by infecting agents residing around international airports. Every month, the simulation updates the genomes seeded around airports, selecting the variant with the highest transmissibility detected during the preceding month.

As described in Supplementary Section C.1, disease is transmitted among agents that interact across different social contexts. The transmission process is simulated in discrete half-day time steps: “daytime” cycles during which agents interact in workplaces or educational settings (e.g., class, grade, school), and “nighttime” cycles during which agents interact in residential settings (e.g., household, household cluster, neighbourhood, and community). Each agent progresses through several health states: Susceptible, Infectious (asymptomatic or symptomatic), and Recovered, following the natural history of the disease.

At simulation cycle n , the infection probability $p_i(n)$ for a susceptible agent i is determined across all its social contexts $g \in G_i$ (see Supplementary Section C.1.1):

$$p_i(n) = 1 - \prod_{g \in G_i(n)} \prod_{j \in A_g \setminus \{i\}} (1 - p_{j \rightarrow i}(n, g)) \quad (2)$$

where $G_i(n)$ denotes the set of all social contexts g that agent i interacts with during the time cycle n , $A_g \setminus \{i\}$ denotes the set of agents in g (excluding agent i), and $p_{j \rightarrow i}(n, g)$ denotes the probability of infection transmission from infectious agent j to susceptible agent i within their social context $g \in G_i(n)$. The probability $p_{j \rightarrow i}(n, g)$ is defined as follows:

$$p_{j \rightarrow i}(n, g) = K(s_j) f_j(n - n_j) q_{j \rightarrow i}(g) \quad (3)$$

where $q_{j \rightarrow i}(g)$ is the age-dependent interaction probability within g (see Supplementary Section C.1.1); n_j denotes the infection onset time for agent j ; the agent-specific function $f_j(n - n_j)$ is the natural history of the disease, reflecting the infectivity of agent j as its infection progresses (see Supplementary Section C.1.2); and $K(s_j)$ represents the transmissibility of pathogen variant s_j , proportional to the corresponding basic reproductive number R_0 , i.e., $K(s_j)$ is the fitness of genome s_j carried by agent j , as defined by equation (1).

Once susceptible agent i becomes infected, it is possible to assign (i.e., identify) a specific infectious agent as the source of infection. This is simulated by weighted randomly sampling an infection source from all potential infectious agents j across all social contexts $g \in G_i(n)$ in which agent i interacted during this cycle. Then the pathogen genome profile s_j (carried by the identified infection source agent j) is copied to agent i (see Supplementary Section C.1.1).

Various interventions may change the infection probabilities across social contexts. Modelling non-pharmaceutical interventions (NPIs) is described in Section C.2.

4.2.3 Immunological layer (D)

The immunological layer simulates a vaccination rollout, including vaccination coverage, schedule and rates, given vaccine efficacy. Furthermore, the immuno-epidemiological model quantifies the agent immunity resulting from multiple immunity-boosting events (i.e., vaccinations and infections), as described in Supplementary Section D.1. In this work, we broaden the concept of “hybrid immunity” to “compound immunity”, in order to capture non-linear immunity accumulation over various combinations of prior vaccinations and infections. Compound immunity may result from one or multiple vaccinations, one or multiple past infections, or a combination of both vaccination(s) and past infection(s) [27].

We decompose the compound immunity via three separate sub-components, quantifying reductions of different risks: susceptibility, symptomatic infection, and forward transmission. For example, the compound immunity against symptomatic infection, denoted M_i^c , for susceptible agent i interacting with infectious agent x , is defined as follows:

$$M_i^c(n, H_i, s_x) = \min \left(\sqrt{\sum_{r \in H_i} [m_i^c(n, r, s_x)]^2}, 1 \right) \quad (4)$$

where $m_i^{\xi}(n, r, s_x)$ is the immunity against symptomatic infection induced by past immunological event r (vaccination or infection); H_i is the immunological history formed by past records r up to cycle n ; and s_x is the genome carried by infectious agent x . In addition, the compound immunity wanes over time and depends on the genetic distance (see equation (12) in Supplementary Section D.2.1). Supplementary Section D.2 provides more details accounting for different vaccine efficacy components contributing to the compound immunity, and its effects on infection probabilities.

4.3 Phylodynamic measures

4.3.1 Hamming distance

In this study, we used Hamming distance as the primary measure to count nucleotide differences between two genomes [35]. The average reference Hamming distance between evolved genomes and the reference genome (i.e., ancestral genome), denoted \widehat{D} , is used to account for the mutations accumulated during the simulation timeframe, while the average pairwise Hamming distance among evolved genomes, denoted \overline{D} , is used to quantify the genomic diversity. The computation of these two measures is described below.

To quantify the accumulated mutations \widehat{D} , for each simulated day n :

- Select all genome profiles obtained within a one-week forward window starting on day n .
- For each of the profiles, record the number of differences against the reference genome (i.e., ancestral genome, NCBI GenBank accession number MN908947 [36, 17]), producing the reference Hamming distance.
- Compute the average reference Hamming distance across all circulating variants.

To quantify the genomic diversity \overline{D} , for each simulated day n :

- Randomly select 10,000 pairs of profiles obtained within a one-week forward window starting on day n .
- For each pair of genomes, record the number of differences between them as the pairwise Hamming distance.
- Compute the average pairwise Hamming distance of all pairs.

Figures 2 and 3 trace the reference and pairwise Hamming distances for actual SARS-CoV-2 sequence data [15].

In order to trace Hamming distances for the simulated dynamics we followed slightly altered workflows, without applying the weekly windows for genome selection. When dealing with actual sequence data, these windows were needed to filter out sampling inconsistencies. Simulated data include pathogen genomes from all detected hosts, sampled on each simulation day, thus reducing sampling inconsistencies. The reference Hamming distance \widehat{D} was computed against the simulated ancestral strain, constructed for each realisation (as described in Section 4). Figures 7, 9 – 11 trace the reference and pairwise Hamming distances for the simulated phylodynamics.

4.3.2 Statistical stationarity tests

To examine stationarity of the pairwise Hamming distance, we performed statistical stationarity tests, specifically Augmented Dickey-Fuller (ADF) test and one-sided Cumulative Sum (CUSUM) analysis. This allowed us to identify saltations as punctuated changes in the pairwise Hamming distance, which have been found to be closely related to the emergence and dominance of pathogen variants [13].

ADF test. An ADF test detects the presence of unit root [37]. We use the following null and alternative hypotheses to determine stationarity:

H_0 : Pairwise Hamming distance is non-stationary.

H_1 : Pairwise Hamming distance is stationary.

We computed p-value from the ADF test and compared it against a chosen significance level (i.e., 0.05), with p-value smaller than the significance level rejecting H_0 and confirming stationarity. Results of ADF are shown in Supplementary section F.2 and Fig. 27.

CUSUM. A one-sided Cumulative Sum (CUSUM) control chart [38, 39] can identify *anomalies* in the observed time series. In this study, we applied CUSUM on pairwise Hamming distance as shown in Fig. 10.

Let $W(n)$ be the pairwise Hamming distance on day n , with the mean μ and standard deviation σ . We converted $W(n)$ into *high* CUSUM (S^X) and *low* CUSUM (S^Y), as follows:

$$S^X(n+1) = \max(0, S^X(n) + W(n+1) - \mu - \sigma) \quad (5)$$

$$S^Y(n+1) = \max(0, S^Y(n) - W(n+1) + \mu - \sigma) \quad (6)$$

where $S^X(0) = S^Y(0) = 0$.

The high and low CUSUM values, S^X and S^Y , are traced in Fig. 10. We then applied a positive peak detection in S^X and S^Y (i.e., considering CUSUM value greater than 0), to detect the anomalies. Specifically, the peaks identified in S^X indicate the emergence of a more transmissible variant, whereas the peaks identified in S^Y indicate the dominance of a variant within the population. The number of dominant variants is equivalent to the total number of peaks detected in both S^X and S^Y .

We note that CUSUM is a simplified approach and can only identify one variant of concern during a defined period. In other words, it cannot trace the frequency of multiple co-circulating variants and the associated transitions.

Declarations

The authors declare no competing interests.

Data availability

Simulation and post-processing data are available at Zenodo: [10.5281/zenodo.14279413](https://zenodo.org/doi/10.5281/zenodo.14279413).

Code availability

The source code of PHASE TRACE is available at Zenodo: [10.5281/zenodo.14279368](https://zenodo.org/doi/10.5281/zenodo.14279368).

Acknowledgement

This work was supported by the Australian Research Council grant DP220101688 (MP, QDN, SLC, VS, TS). The simulations involved in this work were carried out on the high-performance computing cluster (Artemis) provided by the Sydney Informatics Hub at the University of Sydney. The authors would like to thank Christina M. Jamerlan, Tim Germann, Sara Del Valle, Michael Lachmann, Stuart Ridge, and Stuart Kauffman for many insightful discussions and comments. The authors are also grateful to Oliver Cliff, Cameron Zachreson and Nathan Harding for contributing to the development of AMTraC-19, a predecessor of PHASE TRACE.

Overview of Supplementary Materials

The phylodynamic agent-based model implemented in PHASE TRACE synthesises two parts: the within-host evolution using a phylogenetic model, and the inter-host transmission using a high-resolution agent-based model. This simulator comprises four processing layers: (A) Phylogenetic, (B) Demographic, (C) Epidemic, and (D) Immunological, each with various data flows updating core attributes of *Agent* objects. These agent attributes include: (i) health status, (ii) genome representation of the pathogen if infected, (iii) the social groups with which an agent may interact, and (iv) immunological history of past infections and vaccinations. The PHASE TRACE architecture is described in Methods (subsection 4.1).

The processing layers are detailed in Supplementary Materials as follows:

- (A) Phylogenetic Layer: Section A (Phylogenetic model) describes the model of the within-host evolution.
- (B) Demographic Layer: Section B (Artificial population) details the generation and structure of the artificial heterogeneous population.
- (C) Epidemic Layer: Section C (Multi-strain transmission and control) describes the disease transmission model in terms of agent interactions, in presence of multiple co-circulating pathogens characterised by different genomes (subsection C.1), as well as the control model of multiple non-pharmaceutical interventions and their impact on disease transmission (subsection C.2).
- (D) Immunological Layer: Section D (Immuno-epidemiological model) details modelling of vaccination roll-outs and vaccine-induced immunity (subsection D.1), followed by a description of how the immunity changes over time during pathogen transmission and evolution (subsection D.2). This section also describes how the within-host pathogen evolution affects inter-agent infection transmission, under the effect of compound and waning immunity generated by the immunological history.

Supplementary Materials also include some additional results (Section E), sensitivity analysis (Section G) and details on the computational complexity and implementation of PHASE TRACE (Section H).

A Phylogenetic model

A key part of PHASE TRACE is a phylogenetic model developed to simulate pathogen evolution under diverse selective pressures. The phylogenetic model is incorporated within an agent-based model (ABM) of multi-strain epidemic transmission and control (detailed in Section C.1), and consists of five key components:

- Genome structure represented by a nucleotide sequence with positions assigned to different functions (Section A.1).
- Point mutations occurring at a rate that is averaged across the genome (Section A.2).
- Pathogen fitness determined based on amino acids at specific regions of the genome (Section A.3).
- Infected host categories, differentiating between typical infected hosts and chronically infected hosts (Section A.4).
- Within-host (or intra-host) selective pressure generating advantageous pathogen mutations (Section A.5).

These components capture complex evolutionary dynamics relating selective pressures, mutations, and varying levels of immune response emerging in the heterogeneous host population facing various disease scenarios.

In this study, we calibrated the model to match viral characteristics and epidemic dynamics of SARS-CoV-2, using the COVID-19 pandemic as a case study. This model can be adapted to explore the evolutionary dynamics of other pathogens causing communicable diseases.

A.1 Genome structure

Each infected agent (i.e., host) is assigned an artificially constructed genome. Importantly, the simulated genome is designed to model evolutionary dynamics but is *not* mapped to real features of the viral genome such as known coding

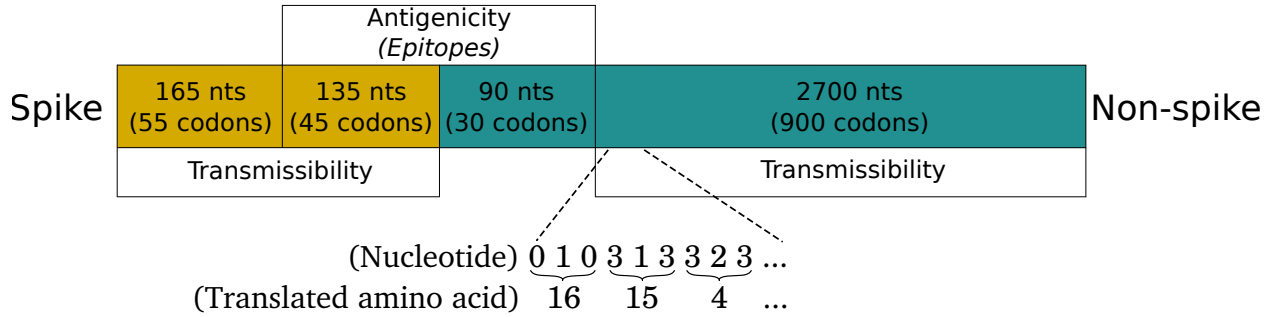


Figure 13: Simulated genome structure consisting of 3,090 nucleotides (nts), equivalent to 1,030 codons. The genome is partitioned into spike (orange) and non-spike (blue) regions. Additionally, the nucleotides can be grouped according to functions: (i) regions consisting of 1,000 codons (100 from spike region and 900 from non-spike region), contributing to the pathogen fitness and the resultant transmissibility; and (ii) regions consisting of 75 codons (45 from spike region and 30 from non-spike region) contributing to antigenicity (i.e., epitopes). The inset displays examples of grouping nucleotides into codons followed by translation to amino acids. For example, nucleotides 0 1 0 form a codon, which is translated as amino acid 16.

sequences, epitopes, or viral functions. Furthermore, for reasons of computational efficiency, we simulate a sequence of only 3,090 nucleotide positions, approximately 10% of the true size of the viral genome [17]. For simplicity, we model only one viral genome per host at any given time step, i.e., we assume that a single viral population dominates in the host, and there is a narrow transmission bottleneck [31].

Each nucleotide position in the simulated genome is represented by a number between 0 and 3. Every three nucleotides is interpreted as a codon (3,090 nucleotides correspond to 1,030 codons, see Fig. 13), encoding a sequence of amino acids following the standard translation rules [40]. We annotate the 20 known amino acids by numerical labels from 0 to 19 instead of the conventional letters [40]. Although we model translation to an amino acid sequence, we do not look for coding regions or otherwise interpret or annotate the simulated sequence in the context of the real virus.

The simulated genome is partitioned into two distinct regions (Fig. 13): the “spike” region (consisting of 100 codons) and the non-spike region (consisting of 930 codons). This partitioning affects only two aspects of the simulation: (1) vaccine-related selective pressure is restricted to the spike region, and (2) mutations in the spike region have a greater chance of enhancing transmissibility (Supplementary Section A.3). 75 codons (45 codons in the spike region and 30 codons in the non-spike region) are interpreted as epitopes relevant for modelling of immunity [41, 42]. 1,000 codons (including 45 that are also in epitopes) are interpreted as relevant to transmissibility. Section D.2.3 provides more details.

A.2 Mutations

In this study, we model mutations as random substitutions at single nucleotide positions. We do not consider insertions, deletions, recombination, or other structural changes to the genome. Fitness and antigenicity are computed from the amino acid sequence, meaning that synonymous nucleotide substitutions will not result in a functionally different simulated genome. We also assume that the transmissibility and antigenicity of viral variants can be computed based on independent contributions from each mutation with respect to the ancestral strain.

In each half-day simulation cycle, the total number of mutations (L) in each of the viral genomes within infected hosts is sampled from a Poisson distribution. The mean of the distribution is set based on an average mutation rate of 0.001 per nt per year across the genome, i.e., $3090 \times 0.001 / (365 \times 2) \approx 0.00423$. The average mutation rate was chosen within the reported range for SARS-CoV-2 of 0.000219 to 0.0012 per nt per year [43, 31]. The relationship between mutations and their contribution to fitness is described in Supplementary Section A.3.

A.3 Contribution to fitness

Individual mutations in the genome affect the overall viral fitness, resulting in growing transmissibility and higher reproductive number (R_0) [16, 44, 45]. Obermeyer et al. [16] assessed the relative fitness of SARS-CoV-2 lineages

(measured as the fold increase in R over the ancestral strain) by linearly combining fitness contributions of individual amino acid substitutions, some of which were found to be fitness-increasing and recognised as spike mutations and non-spike mutations within the nucleocapsid and nonstructural proteins. Additionally, Thadani et al. [45] identified a general distribution of amino acid selection at each position in SARS-CoV-2 sequences and highlighted positions that are prone to viral escape and mutations.

Informed by these studies, we employ a weight table to quantify the individual contributions to fitness of amino acids at each codon position. The overall fitness of a strain, determined by its genome, is modelled as the sum of these individual contributions. This approach allows us to determine fitness of any simulated genome with arbitrary mutations. Specifically, the table assigns a weight $a_{i,j}$ for each of the $N = 1,030$ codon positions and $N_A = 20$ types of amino acids. For the COVID-19 case study, we assigned the weights as follows:

- sample $\mathcal{N}(0, 0.085)$ for $i \in [0, 99]$, the spike region,
- 0 for $i \in [100, 129]$, the non-spike epitopes, and
- sample $\mathcal{N}(0, 0.07)$ for $i \in [130, 1029]$, the non-spike region.

Here, we chose a higher-variance distribution for the weights in the spike region so that those codons have a higher probability of contributing to the viral fitness relative to the non-spike region. This is based on the observation of a higher substitution rate in the spike region compared to other positions [46, 47].

Figure 14 shows a section of the weight table (the first 26 codon positions). The weight table generated for a simulation regulates the pathogen’s evolution. In the absence of other pressures, one would expect substitutions that increase fitness to be preferentially fixed as a simulation progresses, leading to a gradual increase in transmissibility. Using the weight table, we calculate the overall fitness K of genome s by combining the individual contributions of the present amino acids:

$$K(s) = \sum_{i=0}^{N-1} a_{i,s(i)} \quad (7)$$

where $a_{i,s(i)}$ is the fitness contribution of amino acid $j = s(i)$ located at codon position i , with $j \in [0, N_A - 1]$. We note that $a_{i,s(i)}$ can be zero, positive, or negative, representing mutations of neutral, advantageous, or disadvantageous contribution to pathogen fitness.

Prior to simulating the COVID-19 case study, we generated a genome for the ancestral SARS-CoV-2 strain sampled such that its viral fitness, calculated using Eq. 7 and the weight table, fell between 2.65 and 2.85, matching the transmissibility range of the ancestral SARS-CoV-2 strain modelled in our previous work [6]. We used this ancestral genome as a starting point from which other variants originate, thus assuming a shared ancestry for all variants [48, 49]. To optimise memory usage, given the high number of simulated infections, each strain is represented by a list of mutations against the ancestral genome instead of a full-length genome.

A.4 Infected host categories

Host factors, including individual variation in immune response, are known to strongly affect epidemic progression [50, 51]. In particular, chronic carriage of SARS-CoV-2 by immunocompromised hosts is thought to have had a key role in the emergence of new viral variants during the pandemic [31]. In a host with compromised or suppressed immune function, the virus is subjected to different selective pressures and within-host dynamics. A host immune system that is not able to effectively clear the virus is likely to result in a longer infection duration, a higher viral load within the host, and a greater diversity of viral sub-populations [31]. These conditions may facilitate more substitutions and larger increases to viral fitness (saltational evolution) compared to evolution of the virus over the same interval of time when transmitted by a chain of typical hosts and subjected to transmission bottlenecks and competent immune systems. In the case of SARS-CoV-2, chronically infected hosts can have a prolonged recovery period of several months, compared to one to two weeks for typical infected hosts [52, 46].

To examine the possible role of chronic infections on the pathogen evolution, we differentiate between two infected host categories: chronically infected hosts and the typical infected hosts. The main distinctions include the following aspects: (i) chronically infected hosts are assigned a different natural history model with a significantly longer recovery period, randomly sampled from a uniform distribution ranging from 60 to 370 days reported in many studies (Fig.

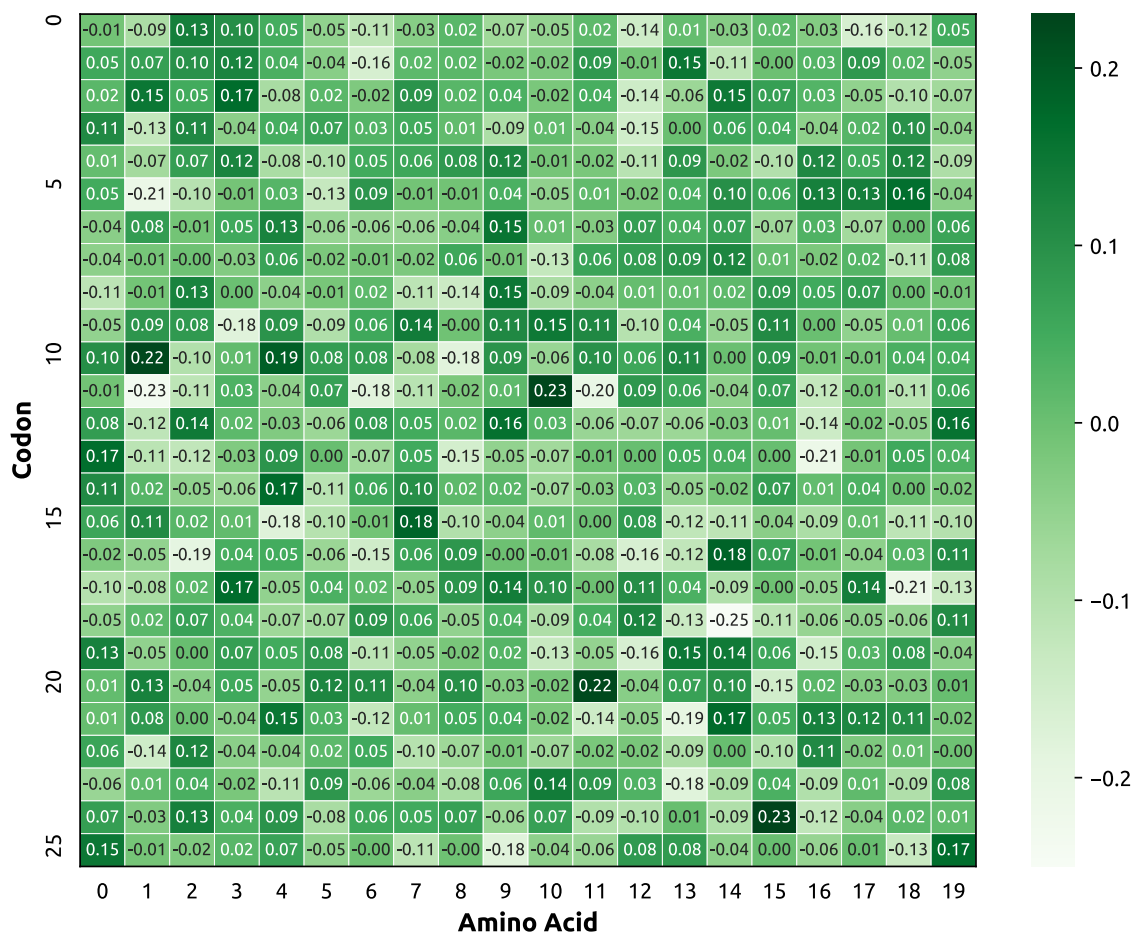


Figure 14: A section of the weight table that quantifies the fitness contributions of 20 amino acids across the genome. Only the first 26 codon positions (vertical axis) are shown for illustrative purposes. Each cell value indicates the potential contribution from each amino acid if present (horizontal axis) at the corresponding codon position (vertical axis). The cell values are sampled from a normal distribution with a mean of 0 (i.e., most random mutations are neutral). Cell colour indicates the magnitude of fitness, with darker colour representing fitness increase and lighter colour representing fitness decrease.

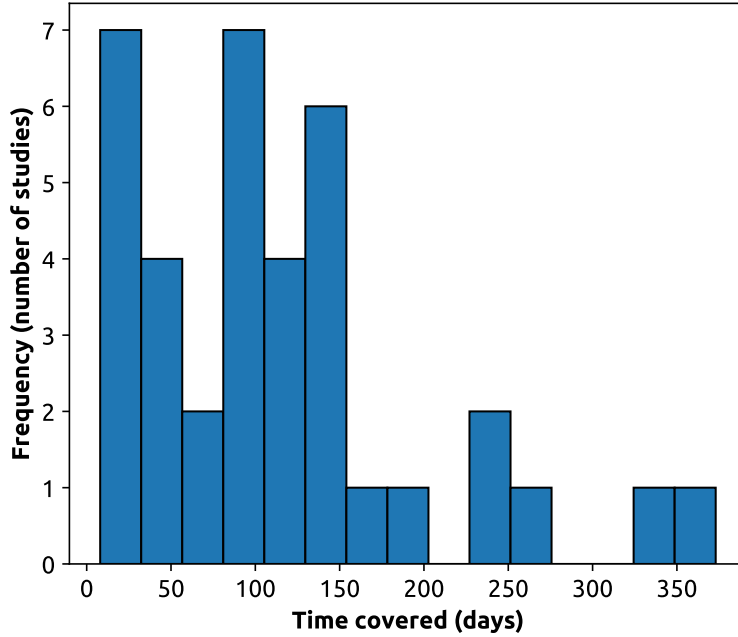


Figure 15: Histogram of infection period of the COVID-19 cases reported by various studies. Datasets were obtained from [53, 54], updated as of December 25, 2022.

15)[46, 53, 54], and (ii) chronically infected hosts may have a higher intra-host selective pressure (detailed in Section G).

Ghafari et al. [46] reported that chronically infected hosts make up a small fraction of the infected hosts (between 0.1 and 0.5% of COVID-19 infections), and only 32% of these hosts may experience strong positive intra-host selection. Considering the high attack rate of the COVID-19, we assume that 0.1% of the entire population is susceptible to chronic infection with COVID-19. We also assume a stronger within-host selective pressure in chronically infected agents, compared to typical infected hosts.

To evaluate the model robustness and quantify the impact of the chronically infected hosts on the overall phylodynamics, we performed sensitivity analysis varying the percentage of chronically infected hosts between 0% to 5% (see Supplementary Section G).

A.5 Intra-host (within-host) selective pressure

The emergence of new variants requires mutations with a fitness advantage capable of breaking through the transmission bottleneck [31]. Mutant strains require time to replicate and out-compete other viral sub-populations within the host in order to be transmitted onwards to other hosts. The selection dynamics within the host are influenced by host characteristics and the length of infection [53, 31, 46].

A virus that has less opportunity to develop within-host diversity will be less effective at exploring the fitness landscape. We emulate this by biasing the fitness of mutant sequences generated from a parent sequence. At each time step where we need to generate mutations in the viral sequence associated with an infected host, we first independently generate M candidate sequences and rank them by their fitness. We then sample one sequence from the top $X \leq M$ candidates to be the new sequence. The difference $M - X + 1$ specifies the selective pressure strength. For example, if $M = X$, this is equivalent to generating only a single candidate sequence, indicating a weak selective pressure. On the other hand, if $M = 100$ and $X = 1$, then the selected sequence will be the fittest of 100 randomly generated candidate sequences, indicating a strong selective pressure and bias towards higher fitness. In other words, small values of X imply more efficient exploration of the fitness landscape as might be expected during a chronic infection. This mechanism emulates within-host dynamics that are not explicitly modelled, since each infected agent is associated with only a single viral

genome at each simulation cycle.

Each cycle, for every infected host agent carrying genome s and acquiring L independent mutations (governed by the mutation rate as described in Section A.2), we simulate the within-host selective pressure through a three-step procedure:

1. Randomly generate $M - X + 1$ mutated genome sequences by independently selecting and changing L positions in sequence s for each, by substituting the corresponding nucleotide number by a uniformly sampled number between 0 and 3. These generated mutated genome sequences become candidates for the upcoming selection process.
2. Compute the fitness of each of the $M - X + 1$ generated mutated genome sequences using the fitness weight table (see Section A.3). Rank these generated mutated genome sequences by fitness in descending order.
3. Select the genome sequence with the highest rank (fittest) among the generated mutated genome sequences. Replace s by this selected sequence.

At the start of their infection, both typical infected hosts and chronically infected hosts are processed using the described selective pressure procedure with the same selective strength X where $X \lesssim M$ (representing low selective pressure). However, beginning from 60 days post-infection, we differentiate chronically infected hosts by assigning them a higher selective strength (i.e., $X \ll M$). In comparison, by this point typical infected hosts have already recovered. This setup aligns with the observation that a 60-day post-infection interval is observed before the intra-host pressure begins to impact the SARS-CoV-2 transmission bottleneck significantly [31, 46]. We note that chronically infected hosts have a lengthened recovery period between 60 and 370 days (see Section A.4), and the described selection process continues until the host recovers.

B Artificial agent-based population

Prior to the simulation, we stochastically generated three distinct artificial populations of anonymous agents (corresponding to layer (B) Demographic shown in Fig. 12), used to examine evolutionary and epidemiological dynamics:

- (large) approx. 25.4 million, comparable to the Australian population;
- (medium) approx. 8 million, comparable to the population of New South Wales (a relatively population-dense state in Australia);
- (small) approx. 1.7 million, comparable to the population of South Australia (a relatively population-sparse state in Australia).

We selected these population sizes for two reasons: (i) to investigate the relationship between the population size and phylodynamics, and (ii) to ensure computational feasibility. These considerations are based on the observation that the SARS-CoV-2 variants of concern may have emerged in countries of different population sizes (e.g., South Africa, with a population of approximately 59 million; UK, with a population of around 56 million; and Botswana, with a population over 2.4 million). In addition, our preliminary test simulations revealed that the computational cost increases non-linearly with the population size (see Section H). In this study, we focus on revealing the representative evolutionary characteristics of SARS-CoV-2, while maintaining computational efficiency by using the three populations listed above. However, given sufficient computational resources, much larger populations (e.g., over one billion population representing countries such as India) may also be generated in order to quantify the impact of population size on phylodynamic and disease dynamics.

The constructed artificial population captures essential demographic characteristics and commuting patterns represented in the latest Australian census and other datasets, as well as agent-to-agent interactions in various social mixing contexts, thus representing the population heterogeneity. Specifically, we generated the artificial population using demographic and travel data sourced from the Australian Bureau of Statistics (ABS) 2021 Census [32], international air traffic reports (detailing incoming passenger flows at Australian airports) [55], and educational registration records (including data on schools and students) [56]. Each agent in the artificial population was assigned multiple demographic attributes, such as age, gender, and residency location, alongside social mixing contexts across various settings: residential (e.g., household, household cluster, neighbourhood and statistical area which maps to a local government area), educational (e.g., classroom/school for agents aged 18 years or younger), and workplace (for agents aged over 18 years). Figure 5 provides a visual representation of the considered social mixing contexts. For each agent, the

residential contexts are determined based on residential demographics, while the workplace and educational contexts are assigned based on commuting patterns (commute to work and class/school, depending on the agent’s age group).

The population generation used by PHASE TRACE can also cover a specific geographical area. In other words, in addition to an artificial population matching the demographics of the entire Australian population, it is possible to generate smaller populations corresponding to individual states and territories, while maintaining their demographic attributes and travel patterns. The population generation algorithm resolves several known discrepancies (introduced by privacy-protection algorithms employed by government agencies), and maintains integrity across different public datasets [25, 24]. A detailed description of the population generation methodology and the population data structure can be found in the Supplementary Materials of a prior study [24] and the user guide of our open-source software [57].

C Multi-strain transmission and control

C.1 Multi-strain transmission model

The multi-strain transmission model of PHASE TRACE stochastically simulates pathogen transmission between hosts (Epidemic Layer shown in Fig. 12). This model introduced several new features to our previous ABM, AMTraC-19 [6, 23, 26, 24]. In this section, we describe how transmission is affected by the genome model described above.

At the start of the simulation, all agents in the population are susceptible. Initial infections carrying the generated ancestral genome are seeded in metropolitan statistical areas (around international airports) as imported cases. These seeding events occur periodically throughout the simulation. The viral genome of the imported infections is taken to be the variant with the highest transmissibility from the preceding month of simulation, with additional mutations randomly added (using a weak selective pressure, see Table 4) to represent the evolution of the virus outside of the simulated population.

From the initial infections, the pathogen propagates through the population as susceptible and infected agents interact. These interactions occur in various social contexts in discrete half-day time cycles. During “daytime” cycles, agents interact in workplaces or educational settings (e.g., class, grade, school). “Nighttime” cycles instead involve interactions in residential settings (e.g., household, household cluster, neighbourhood, and community). Weekdays consist of a daytime cycle and a nighttime cycle, whereas weekend days consist of two nighttime cycles (i.e., no interactions in workplace/educational contexts).

A transmission event changes the health state of the newly-infected agent from Susceptible to Infectious (asymptomatic or symptomatic). Once the infection is cleared, the agent transitions to the Recovered state. Recovered agents are again susceptible to re-infection, but any subsequent transition back to Infectious is moderated by the immunity level (see following sections for more detail).

C.1.1 Susceptible-infectious transition

Transmission from agent j to agent i depends on the probability of their interaction, their ages, and the context g in which the agents interact. These daily context- and age-dependent interaction probabilities $q_{j \rightarrow i}(g)$ have been defined and calibrated in previous studies [6, 26]. At cycle n , the transmission probability, $p_{j \rightarrow i}(n, g)$, is determined as follows:

$$p_{j \rightarrow i}(n, g) = K(s_j) f_j(n - n_j) q_{j \rightarrow i}(g) \quad (8)$$

where $K(s_j)$ represents the transmissibility of pathogen variant s_j , proportional to the corresponding basic reproductive number R_0 , i.e., $K(s_j)$ is the fitness of genome s_j carried by agent j , as defined by equation (7); n_j is the time cycle when agent j started experiencing the onset of infection; and the function $f_j(n - n_j)$ determines agent j ’s infectivity over time according to the natural history model. At the time cycle n , agent j ’s infectivity is $0 < f_j(n - n_j) \leq 1$ with the infectivity peak equal to 1. For uninfected agents, $f(\cdot) = 0$. For simplicity, we assume that all variants share the same progression of disease, but differ in their transmissibility (determined by fitness K), and that only one variant can be transmitted during the infection process.

We then extend the scenario to consider the probability of agent i getting infected by interacting with all other agents sharing the same social mixing contexts across all levels at time cycle n , defined as follows:

$$p_i(n) = 1 - \prod_{g \in G_i(n)} \prod_{j \in A_g \setminus \{i\}} (1 - p_{j \rightarrow i}(n, g)) \quad (9)$$

where $G_i(n)$ is the set of social mixing contexts where interactions between agent i and other agents may occur (depending on factors such as weekday or weekend, daytime or nighttime), and $A_g \setminus \{i\}$ is the list of all agents in the context $g \in G_i(n)$ except agent i . We shall expand Equation 9 in later sections to incorporate the effects of non-pharmaceutical interventions (Equation 11) and effects of immunity (Equation 20).

Eq. 9 defines the infection probability for agent i interacting with other infected agents across all of its social contexts. However, this probability is an aggregate of the interactions and does not identify the specific source of infection, which must be known in order to copy its viral sequence to the newly infected host. We assign the source of infection by constructing a discrete distribution to randomly sample one agent from all potential infected agents j across all social contexts $g \in G_i(n)$ to which agent i belongs. The probability of selecting agent j is given by

$$\frac{p_{j \rightarrow i}(\cdot)}{\sum_j p_{j \rightarrow i}(\cdot)}$$

An infectious agent is either symptomatic or asymptomatic. The probability of being symptomatic, $z_i(n)$, depends on the infection probability $p_i(n)$ and an age-dependent scaling factor σ_i characterising the proportion of symptomatic cases among all infections in the corresponding age group:

$$z_i(n) = \sigma_i p_i(n) \quad (10)$$

where $\sigma_i = \sigma^a$ for adults (age > 18) and $\sigma_i = \sigma^c$ for children (age ≤ 18). The asymptomatic infectious agents have lower infectivity (i.e., lower $f_i(n - n_i)$), compared to the symptomatic agents, which also affects the strength of transmission to other susceptible agents.

Following our prior studies [6, 26, 24], we assumed that only a fraction of total infections, especially asymptomatic infections, are detected daily. In our model, we set a lower detection probability for asymptomatic cases (π') than the symptomatic cases (π), such that $\pi \gg \pi'$. In addition, we assumed that chronically infected cases have the same detection probability as asymptomatic cases. In the COVID-19 case study, we used detection rates of $\pi = 0.13$ and $\pi' = 0.01$, calibrated to the Omicron variant of SARS-CoV-2 [27].

C.1.2 Infectious-recovered and recovered-susceptible transitions

Following the natural history model, an infectious agent recovers after a certain recovery period dependent on the host category (see Section G). We assume that both typical and chronically infected hosts develop infectivity fairly quickly from the onset of infection (following a lognormal distribution). However, chronically infected hosts experience a significantly longer recovery than the typical infected hosts. The natural history model describing the disease progression for both host categories is illustrated in Fig. 16.

For a period of 60 days following recovery, agents are immune to re-infection, consistent with empirical definitions that attempted to distinguish between reinfection and serial testing of an initial infection for SARS-CoV-2 [58, 59]. After 60 days, the immunity induced by infection starts to wane, and the recovered agent becomes susceptible again. The re-infection probability for a recovered agent on subsequent exposure depends on their infection and vaccination history both in terms of the genomic similarity of viral strains and the time elapsed (see Section D.1 for more details).

C.2 Non-Pharmaceutical Interventions

The model includes several non-pharmaceutical interventions (NPIs), such as case isolation (CI), home quarantine (HQ), school closures (SC), and social distancing (SD). The implementation of each NPI is governed by: (i) a macro-distancing parameter determining the population fraction adhering to the intervention (Table 2), and (ii) a set of micro-distancing parameters that quantify the altered (typically decreased) interaction strengths between NPI-compliant individuals in a given social context (Table 1).

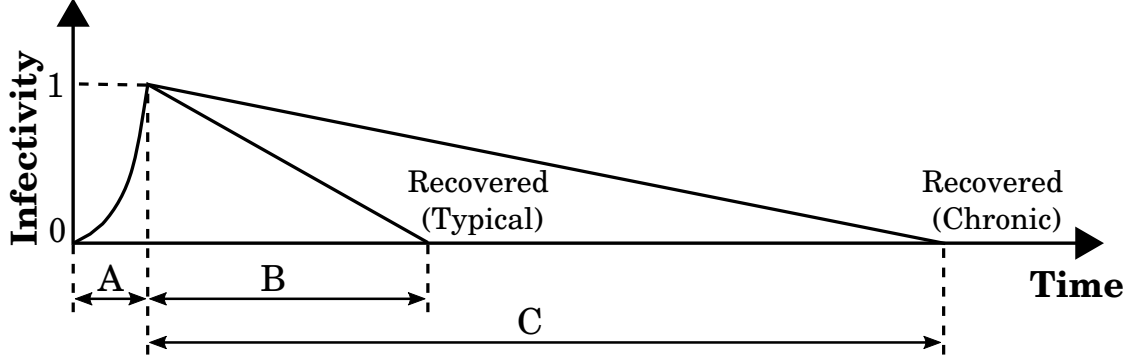


Figure 16: A schematic representation of the natural history describing the SARS-CoV-2 infection progression in an agent. The infectivity initially increases exponentially from the onset of infection, reaching the peak, and subsequently declining linearly to zero until recovery. For each infected host, the duration from the infection onset to the infectivity peak is sampled from a lognormal distribution (A) with parameters $\mu = 1.013$ and $\sigma = 0.413$. The recovery period is sampled from a uniform distribution, ranging from 7 to 11 days (B) for typical infections, or from 60 to 370 days (C) for chronic infections.

Intervention	Micro-distancing (interaction strengths)			Duration t
	Household	Community	Workplace/School	
CI (typical)	1.0	0.25	0.25	$D(i)$
CI (chronic)	0.01	0.0	0.0	$D(i)$
HQ	2.0	0.25	0.25	7 – 30
SC	1.0	0.5	0	dynamic
SD	1.0	0.25	0.1	dynamic

Table 1: The micro-distancing parameters (interaction strengths) for the considered NPIs. The micro-duration of CI is limited by the disease progression in the affected agent i , $D(i)$. Interaction strengths for CI are set to be significantly lower for chronically infected hosts.

Following Eq. 9, the NPI-affected infection probability for agent i without prior infections or vaccinations is given by

$$p_i(n) = 1 - \prod_{g \in G_i(n)} \left[1 - F_g(i) \left(1 - \prod_{j \in A_g \setminus \{i\}} (1 - F_g(j) p_{j \rightarrow i}(n, g)) \right) \right] \quad (11)$$

where $F_g(j)$ denotes the NPI-affected strength of interaction between agent j and other agents in mixing context g . For an agent j adopting NPIs, $F_g(j) \neq 1$, denoting a modified infection probability from agent j . For an agent j not adopting any NPIs, $F_g(j) = 1$.

The assignment of NPI-compliant agents is determined based on a Bernoulli process with the probability specified by the macro-distancing parameters. While an agent may comply with multiple NPIs, their interaction strengths, $F_g(j)$, can only be adjusted to one NPI. We therefore use the parameters for only the first NPI to which an agent complies in the following ordered list: CI, HQ, SD, and SC. The micro and macro-distancing parameters of CI vary depending on the host type, where chronically infected hosts are fully compliant (i.e., macro-distancing level is set to 1.0), with significantly reduced interaction strengths across all social contexts (Tables 1 and 2). This parametrisation agrees with the public health recommendations for chronically infected hosts to take extra precautions to prevent severe illness [60].

We define SD as a broad behavioural-driven NPI that reduces interaction strengths among individuals, due to stay-at-home orders and other measures (including physical distancing, mask wearing, etc.) adopted during (partial) lockdowns. In other words, the SD compliance level can be interpreted as the fraction of the population that follow the restrictions imposed during (partial) lockdowns. We designed an intervention scenario with a dynamically adjustable SD compliance profile representative of NPIs implemented in many countries during the COVID-19 pandemic [26]. Specifically, we set the SD compliance level to gradually decline annually over the 6-year simulation period, from 50% at the start of the pandemic in 2020 to 20% in the endemic stage from 2023 onwards. In addition, the activation of SD was set to be

Intervention	Simulation year			
	2020	2021	2022	2023-onwards
CI (typical)	0.7	0.7	0.7	0.7
CI (chronic)	1.0	1.0	1.0	1.0
HQ	0.5	0.5	0.5	0.5
SC (students/teachers)	1.0	0.0	0.0	0.0
SC (parents)	0.25	0.0	0.0	0.0
SD	0.5	0.4	0.3	0.2

Table 2: The macro-distancing parametrisation (population fractions) for the considered NPIs over the 6-year simulation period for SARS-CoV-2. The CI-compliant population fraction is lower for typically infected hosts than for chronically infected hosts. Students/teachers are assumed to fully comply with SC, while parents of school-aged children have a reduced compliance level.

triggered by a sufficiently high prevalence (e.g., exceeding 200 cases), with SD deactivated once the disease prevalence falls below a certain threshold (e.g., 100 cases). Table 2 and Fig. 5 describe a detailed setup and parametrisation.

D Immuno-epidemiological model

D.1 Vaccination

Following our prior work [22, 26, 24], the model includes a vaccination scheme under which agents are immunised according to an average daily vaccination rate. The vaccination rate is demographically stratified by age, with agents aged 18 to 35 years old vaccinated at a 10-fold higher rate than young or elderly agents, and by immunisation history, with 60% of vaccines going to agents with some history of vaccination [61]. Agents are eligible for vaccination only if they are free from infection for at least three months. We did not model vaccination schedules consisting of multiple doses within a season, instead assuming that a single vaccination event confers the cumulative immunity of the entire recommended dosing regimen in a year.

Vaccinated agents have diminishing levels of protection due to two factors: (i) vaccine escape as circulating variants diverge genetically from the vaccine strain at specific epitopes, and (ii) immunity from vaccination wanes over time. The vaccine used each year in the simulation is chosen to target the dominant variant circulating in the preceding simulated year (starting from 2021). We model only one vaccine type administered at any one time. We assumed that peak immunity occurs immediately after vaccination [62].

We simulated a mass vaccination roll-out with a variable daily vaccination rate updated annually, starting from zero (i.e., no available vaccine) in 2020, rising to 0.147% of the entire population per day in 2021 (when vaccines first became available), and then linearly declining to 0.047% of the population per day in 2026 (Fig. 17).

D.2 Compound immunity and waning effects

Individuals who have been vaccinated and/or experienced prior infections develop immunity against the disease, subsequently reducing their immediate susceptibility to infection [63]. Immunity resulting from both vaccination and natural infection in the same individual, known as hybrid immunity, offers more robust protection compared to immunity derived solely from vaccination or natural infection. Hybrid immunity against SARS-CoV-2, for example, is found to have stronger and longer-lasting immune responses than the immunity granted from vaccination or infection alone [64, 65]. As described in Methods (subsection 4.2.3), we use the term “compound immunity” to encompass immunity due to previous exposures, vaccination, and hybrid immunity [27].

For each agent i with a history H_i containing all vaccination and past infection records $r \in H_i$, we characterise their immunity by two distinct components: (i) compound immunity against symptomatic infection (M_i^c , described in section D.2.1), and (ii) compound immunity against forward transmission (M_i^t , described in section D.2.2). We then integrate the compound immunity into the infection probability in Section D.2.3. These immunity components range between 0 and 1 with zero indicating no immunity and one indicating full immunity.

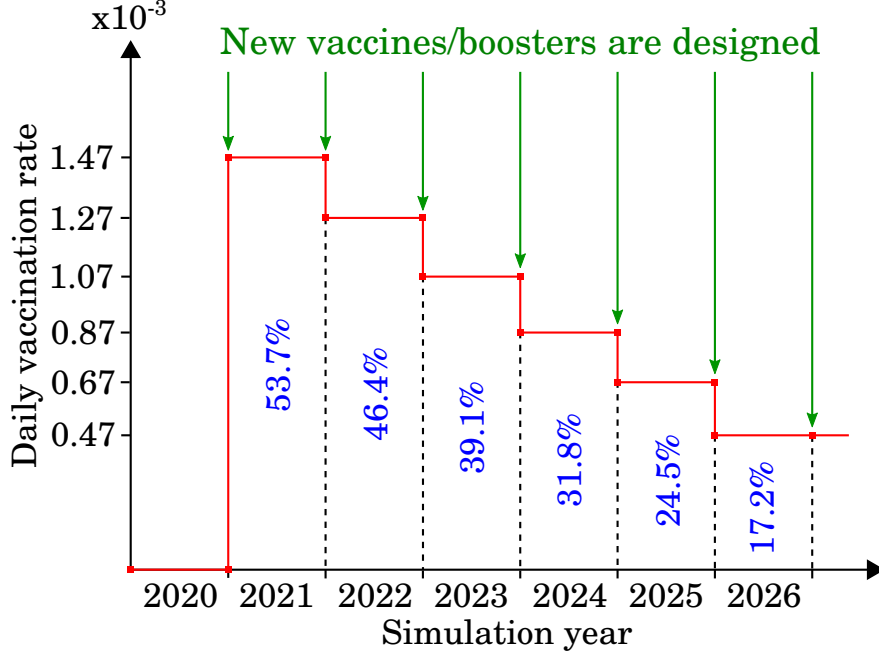


Figure 17: A simulated mass vaccination roll-out with varying daily vaccination rates (y-axis) and multiple boosting events targeted for COVID-19 (green arrows). The percentage (in blue) within each bar represents the approximate percentage of the vaccinated population at the end of the year.

D.2.1 Compound immunity against symptomatic infection

To determine the immunity against symptomatic infection of a susceptible agent i , exposed to a potential infection from an infectious agent x , we need to consider the genome sequence of the variant s_x carried by x . At time cycle n , given a single vaccination or infection record r for agent i , we determine their immunity against symptomatic infection as follows:

$$m_i^c(n, r, s_x) = m^c(r) \left[1 - \min\left(1, \epsilon^c(n - n_r)\right) \right] \left[1 - \min\left(1, \tau \Delta_r(s_x, s_T)\right) \right] \quad (12)$$

where

- $m^c(r)$ denotes the peak immunity against symptomatic infection developed from either vaccination or past infection recorded in r against a target variant with genome s_T (see Table 3),
- ϵ^c is the waning rate of immunity (proportion of immunity lost) against symptomatic infection per simulation cycle,
- $(n - n_r)$ is the number of cycles between the current cycle n and the record cycle n_r ,
- $\Delta_r(s_x, s_T)$ is the genetic distance measured by number of amino acids that differ between genomes s_T and s_x in the epitope regions, either in spike regions only [66, 67] (if r is a vaccination event), or in both spike and non-spike regions (if r is a previous infection) [68],
- factor τ is the immunity reduction per amino acid difference between these two genomes.

Equation 12 shows that m_i^c reduces linearly over time, governed by two constant rates: immunity waning rate ϵ^c over time, and immunity reduction factor τ over genetic distance. This assumption matches observations reported in various studies suggesting a linear reduction between (i) COVID-19 vaccine effectiveness and time [69, 70, 71], and (ii) genetic distance and immune evasion [62]. Figure 18 shows a linear regression fitting of vaccine effectiveness over time for different types of vaccines, constructed using supplementary data from [71]. We note that the waning immunity term can be easily adjusted to follow a non-linear reduction, such as exponential decay [72, 73] or based on a gamma distribution [74].

We then compute the compound immunity for agent i induced by multiple vaccination and/or infection events. The compound immunity against symptomatic infection, $M_i^c(n, H_i, s_x)$, accumulates non-linearly with an upper bound of 1

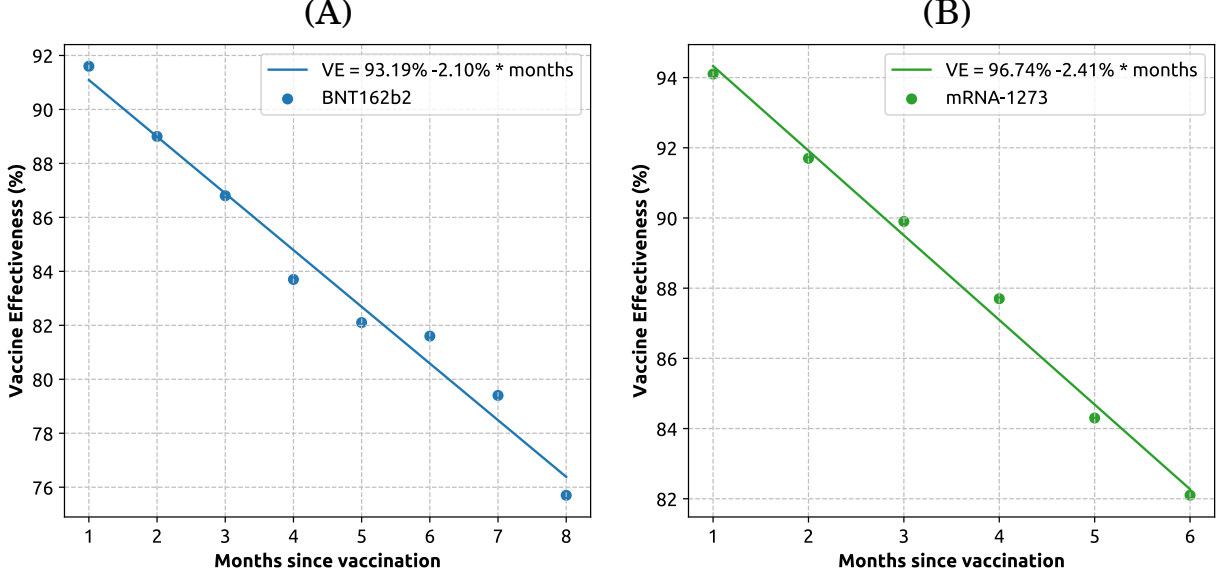


Figure 18: Vaccine effectiveness against infection reduction over time for two widely used mRNA vaccines: (A) Pfizer (BNT162b2), and (B) Moderna (mRNA-1273), plotted and fitted using data from [71]. The equation shown in each plot represents the fitted linear regression for each vaccine, estimating a linear reduction in effectiveness from 2.1% to 2.4% per month.

(i.e., perfect immunity):

$$M_i^c(n, H_i, s_x) = \min \left(\sqrt{\sum_{r \in H_i} [m_i^c(n, r, s_x)]^2}, 1 \right) \quad (13)$$

In our model, the level of protection provided by M_i^c is further decomposed into two components: the immunity against susceptibility (M_i^θ), and the immunity against symptomatic infection given the infection (M_i^ζ). These two components may also be referred to as the susceptibility-reducing immunity and disease-preventing immunity, respectively. Following prior studies [22, 23, 26], we calculate M_i^θ and M_i^ζ as:

$$M_i^\zeta(n, H_i, s_x) = M_i^\theta(n, H_i, s_x) = 1 - \sqrt{1 - M_i^c(n, H_i, s_x)} \quad (14)$$

which satisfies a general relationship:

$$M_i^c(n, H_i, s_x) = M_i^\zeta(n, H_i, s_x) + M_i^\theta(n, H_i, s_x) - M_i^\zeta(n, H_i, s_x)M_i^\theta(n, H_i, s_x) \quad (15)$$

D.2.2 Compound immunity against forward transmission

Following [75, 22, 76], we also consider the immunity component against forward transmission. At time cycle n , for an infected agent i , the immunity against forward infection from one vaccination/infection event, represented by record r , is calculated as follows:

$$m_i^t(n, r) = m^t(r) \left[1 - \min \left(1, \epsilon^t(n - n_r) \right) \right] \quad (16)$$

where $m^t(r)$ denotes the peak immunity against forward transmission developed from either vaccination or past infection recorded in r ; rate ϵ^t is the forward-transmission immunity waning rate per simulation cycle; and n_r is the record cycle of r .

We then consider the compound immunity against forward transmission, accounting for all records in H_i , which follows a non-linear combination of all individual components $m_i^t(n, r)$. Similar to the calculation of the compound immunity against symptomatic infection, we calculate the compound immunity against forward transmission where the upper

bound equals 1 (i.e., perfect immunity):

$$M_i^t(n, H_i) = \min \left(\sqrt{\sum_{r \in H_i} [m_i^t(n, r)]^2}, 1 \right) \quad (17)$$

D.2.3 Incorporating compound immunity in infection probability

Here, we incorporate the compound immunity, against infection (M^θ) and forward transmission (M^t), within the infection probability, extending the NPI-affected probability of infection (Equation 11 in Section C.2).

The impact of compound immunity on infection probability is modelled by distinguishing two factors that affect the infection of a susceptible agent i :

- (\mathcal{P}^I) the impact of forward infection from all infected agents j with whom this agent has contact, affected by M_j^t , and
- (\mathcal{P}^{II}) the agent i 's immunity against infection from these sources, affected by M_i^θ .

We modelled the impact of factors (\mathcal{P}^I) and (\mathcal{P}^{II}) by decomposing the transition from Susceptible state to Infectious state into two consecutive steps:

- (1) considering factor (\mathcal{P}^I) alone, the model identifies whether agent i is *potentially* infected, and if so, it determines the most likely source of this potential infection; and
- (2) considering (\mathcal{P}^{II}), the model ascertains whether infection is *actually* transmitted from this source to agent i .

Step (I). We calculate the probability of agent i becoming *potentially* infected at time cycle n , $p_i^E(n)$, while accounting for NPI-compliance and the immunity against forward infection of other agents, i.e., quantifying factor (\mathcal{P}^I), as:

$$p_i^I(n) = 1 - \prod_{g \in G_i(n)} \left[1 - F_g(i) \left(1 - \prod_{j \in A_g \setminus \{i\}} \left(1 - (1 - M_j^t(n, H_j)) F_g(j) p_{j \rightarrow i}(n, g) \right) \right) \right] \quad (18)$$

where $F_g(j)$ denotes the strength of interaction between agent j and other agents in mixing context g , and $M_j^t(n, H_j)$ represents the immunity against forward transmission based on the history H_j of past infections and vaccinations of agent j . We note that $p_i^I(n)$ accounts for the immunity against forward transmission developed by any agent j sharing a social context with agent i , thus accounting for factor (\mathcal{P}^I).

If agent i is determined to be *potentially* infected according to the Bernoulli trial with $p_i^I(n)$, the source potentially infecting agent i is identified by sampling from a discrete distribution that includes all infectious agents j sharing a social context g with agent i . The probability of selecting an agent j as a potential source of infection from this distribution is given by

$$\frac{(1 - M_j^t(n, H_j)) F_g(j) p_{j \rightarrow i}(n, g)}{\sum_j (1 - M_j^t(n, H_j)) F_g(j) p_{j \rightarrow i}(n, g)}.$$

Step (II). Given the identified source agent e potentially transmitting infection to agent i , the model identifies the corresponding genome s_e , yielding the probability of infection transmission from source e to agent i :

$$p_i^{II}(n, H_i, s_e) = 1 - M_i^\theta(n, H_i, s_e) \quad (19)$$

where $M_i^\theta(n, H_i, s_e)$ is the susceptibility-reducing immunity of agent i with immunological history H_i , determined with respect to genome s_e specifically.

Combining two steps (I) and (II) determines the infection probability for susceptible agent i (i.e., the probability of its transition from Susceptible to Infectious state), in the context of relevant NPI compliance and immunological histories within the population:

$$p_i(n, H_i, s_e) = p_i^{II}(n, H_i, s_e) p_i^I(n) \quad (20)$$

Parameter	Value	Reference/Note
$m^c(r)$	0.7	Peak immunity against symptomatic infection, given prior infection or vaccination record r
ϵ^c	0.00067	Immunity waning rate per day for m^c
τ	0.052	Immunity reduction per amino acid difference in epitope regions
$m^t(r)$	0.4	Peak immunity against infection transmission, given prior infection or vaccination record r
ϵ^t	0.00067	Immunity waning rate per day for m^t

Table 3: Simulation parameters for compound immunity.

Parameter	Value
Genome length, spike region (nucleotide positions)	300
Genome length, non-spike region (nucleotide positions)	2790
Genome length, spike and epitope region (nucleotide positions)	135
Genome length, non-spike and epitope region (nucleotide positions)	90
Mutation rate, spike region (mutations per nucleotide per year)	0.001
Mutation rate, non-spike region (mutations per nucleotide per year)	0.001
Within-host selective pressure, typical infected hosts	$X = 99, M = 100$
Within-host selective pressure, chronically infected hosts	$X = 30, M = 100$
Within-host selective pressure, imported infections	$X = 99, M = 100$
Fraction of chronic infections in the entire agent population	0.001
Fitness of ancestral strain, minimum	2.65
Fitness of ancestral strain, maximum	2.85

Table 4: Phylogenetic parameters used in the SARS-CoV-2 case study.

The probability that susceptible agent i becomes ill (i.e., symptomatic), originally defined in Equation 10, is then updated as:

$$z_i(n, H_i, s_e) = \left(1 - M_i^\zeta(n, H_i, s_e)\right) \sigma_i p_i(n, H_i, s_e) \quad (21)$$

where M_i^ζ is the disease-preventing immunity of agent i , developed as a result of past infections and vaccinations (represented in H_i), determined against the specific source of infection (i.e., the variant characterised by s_e).

Table 3 lists key immunity-related parameters used in the COVID-19 case study. Using a range of reports [77, 78, 79], we assumed that the peak level of vaccine-induced immunity against SARS-CoV-2 infection is comparable to that of natural immunity.

E Parametrisation and additional results

The phylogenetic parameters used in the SARS-CoV-2 case study are summarised in Supplementary Table 4. For an in-depth description of the dynamics simulated with these parameters, refer to Section 2.2. Additionally, see Section A for parameter justification and calibration.

Figures 19 to 22 illustrate simulated epidemic dynamics, as well as the dynamics of transmissibility and mutation accumulation across populations of varying sizes: small (1.7 million), medium (8.0 million), and large (25.4 million). These figures provide insights into population health states, infection and immunisation histories, and viral transmissibility trends, aligned with phylogenetic dynamics observed in different realisations across diverse population scenarios.

Figures 23 to 25 present pairwise Hamming distance dynamics generated using identical phylogenetic parameters across three different population sets. Fig. 23 shows alternative evolution dynamics relative to those shown in Fig. 9 (A, brown dashed line). The high variability of genomic diversity dynamics across different realisations results from the stochastic emergence of variants; hence, we refrain from averaging genomic diversity dynamics across realisations. Nonetheless, the pattern of genomic diversity dynamics aligns well with the trends discussed in Section 2.2, which includes periods of drift, rapid rise, and abrupt collapse. To assess the stationarity of genomic diversity dynamics, we

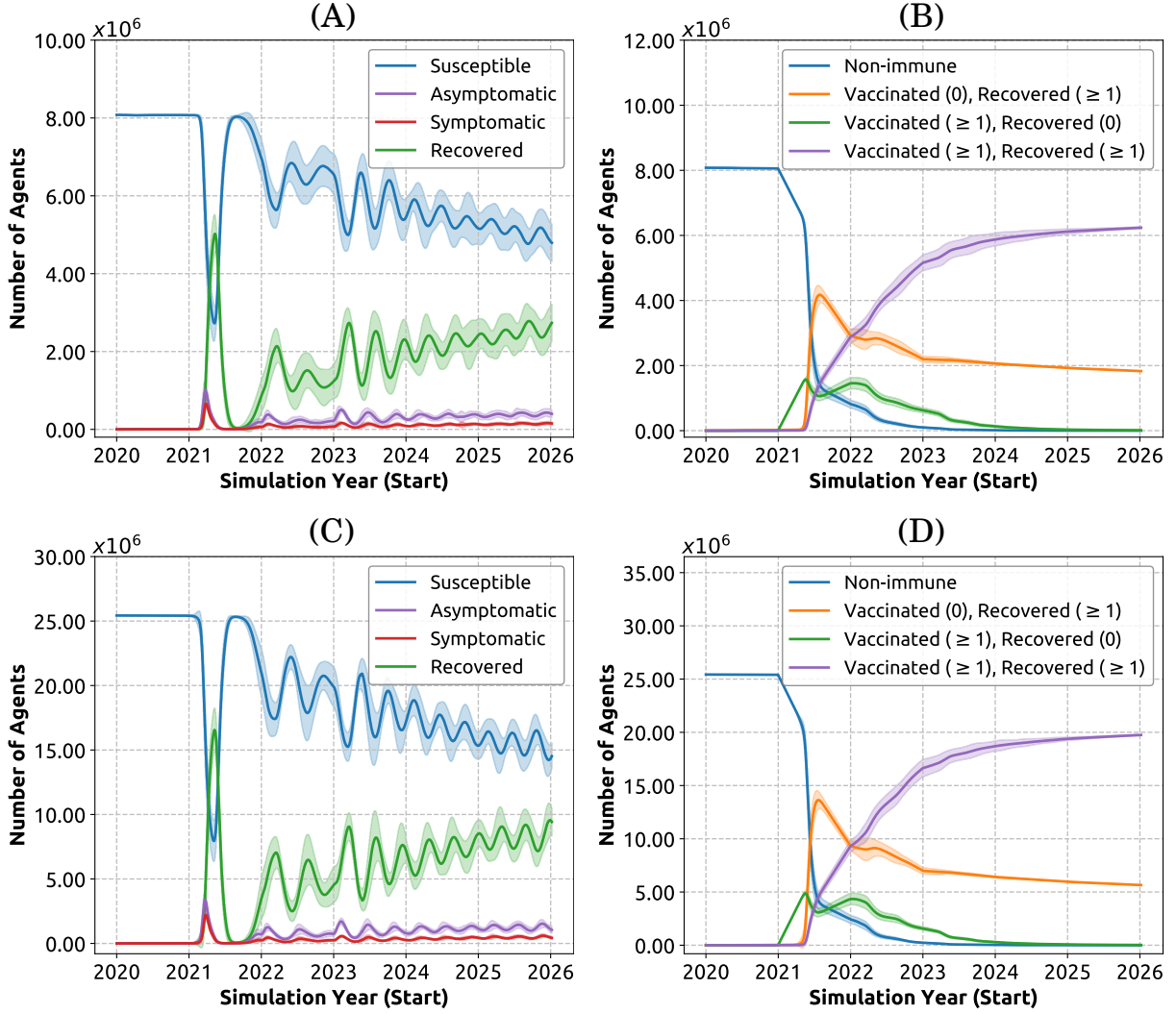


Figure 19: Simulated epidemic patterns (Capability 1) shown as mean (solid line) and standard deviation (shaded area). (A) and (C) Population across different health states, including susceptible (blue), asymptomatically infectious (purple), symptomatically infectious (red), and recovered (green) for the populations of 8 million and 25.4 million, respectively. (B) and (D) Population with different immunisation and infection history for the populations of 8 million and 25.4 million, respectively. Numbers in brackets denote the number of immunological (vaccination or infection) records. Individuals with multiple vaccinations or infections (more than 2) are grouped together for simplicity. The mean and average were obtained from approximately 30 realisations.

performed the Augmented Dickey–Fuller test. Fig. 27 shows that the p-value for stationarity associated with genomic diversity dynamics varies significantly with population size, highlighting the increased difficulty for variants to spread and become dominant in larger populations.

F Counterfactual modelling

In this section, we describe two counterfactual modelling scenarios of SARS-CoV-2: the impact of chronic infections on the SARS-CoV-2 evolution (Section F.1), and the impact of population size on stationarity of the genomic diversity \bar{D} (Section F.2).

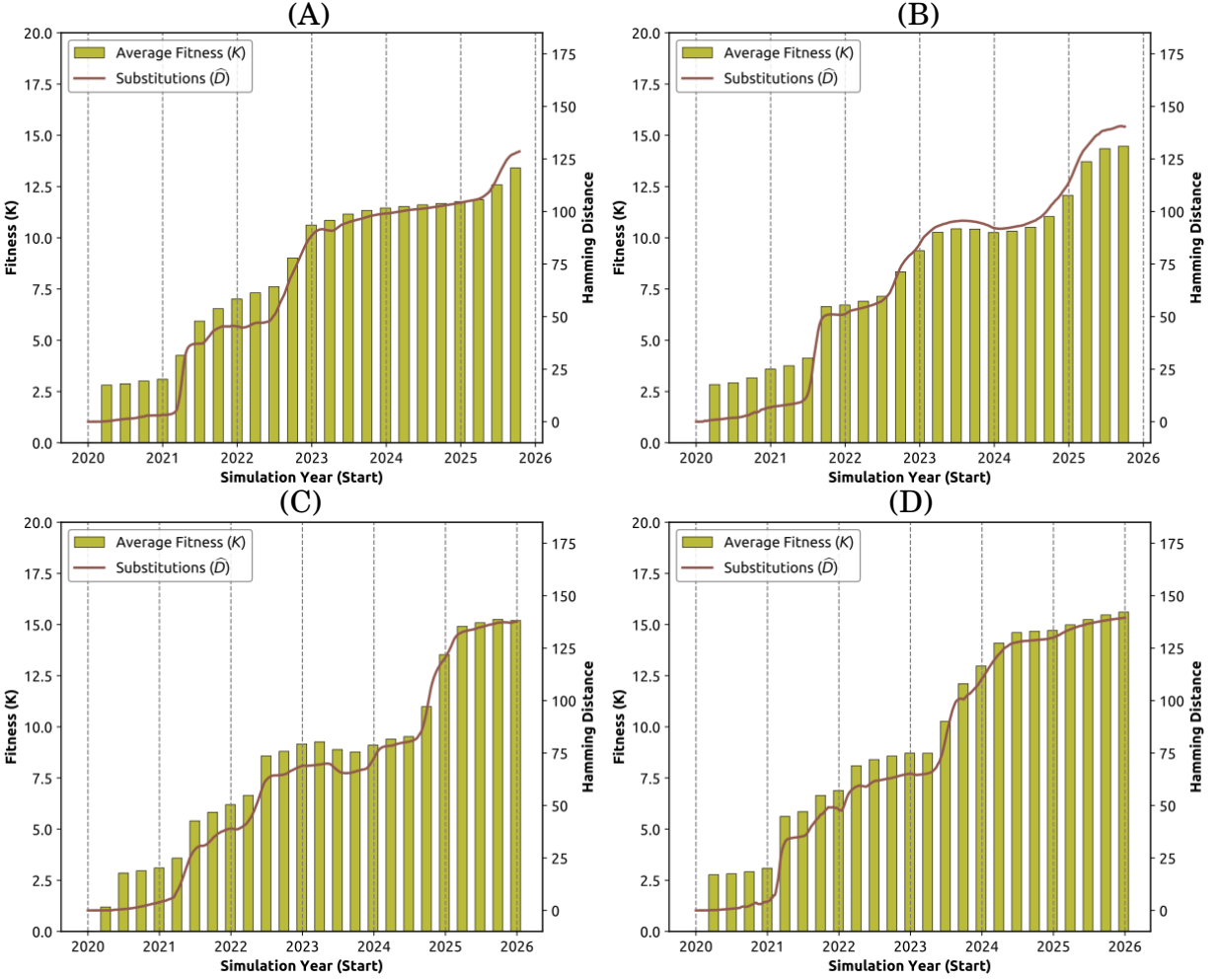


Figure 20: Simulated dynamics of the average transmissibility, i.e., fitness (K , olive bars, y-axis on the left), and the accumulated mutations (\hat{D} , solid brown line, y-axis on the right) for a 1.7 million population from 2020 to 2026. Panels (A)-(D) are profiles plotted using four different realisations.

F.1 Chronic infections

Fig. 26 differentiates between the COVID-19 pandemic simulation scenarios with and without chronic infections. Notably, the absence of chronic infections results in a reduced number of recurrent incidence waves (Fig. 26 (A)) and significantly reduced fluctuations in the genomic diversity \hat{D} , producing lower variability (i.e., a smaller standard deviation) across realisations (Fig. 26 (D)). Furthermore, the growth of both transmissibility (i.e., fitness K) and the accumulated mutations \hat{D} is significantly slower (Fig. 26 (B) and (C)), impeding the emergence of high-fitness variants.

We also explored whether the pathogen phylodynamics are correlated with (1) fractions of chronic infection, and (2) strength of the within-host selective pressure in chronically infected hosts. Fig. 29 shows that a hundred-fold increase in the chronic infection fraction (e.g., from 0.05% to 5% of the population) yields only negligible impact on the incidence curves and phylodynamics. This indicates a ceiling effect of the chronic infection fraction on the incidence, fitness, and accumulated mutations. In contrast, Fig. 30 presents a clear positive correlation between the within-host selective pressure and the phylodynamic characteristics. That is, a higher selective pressure (i.e., selecting top 10% of mutated genome candidates out of their ranked list, $X = 10$, $M = 100$) leads to higher incidence peaks and a more rapid increase in the pathogen fitness and accumulated mutations.

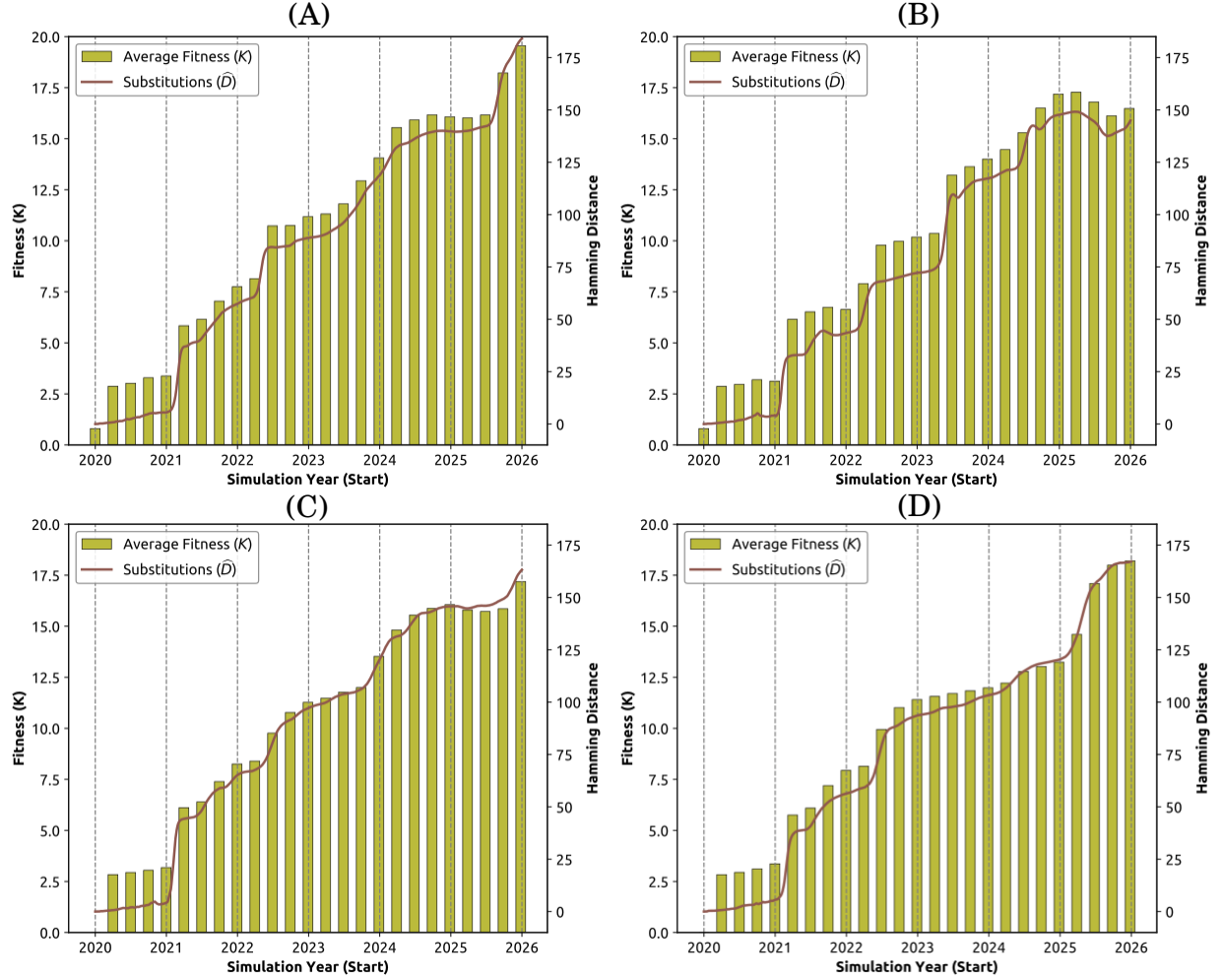


Figure 21: Simulated dynamics of the average transmissibility, i.e., fitness (K , olive bars, y-axis on the left), and the accumulated mutations (\hat{D}), solid brown line, y-axis on the right) for an 8.0 million population from 2020 to 2026. Panels (A)-(D) are profiles plotted using four different realisations.

F.2 Stationarity of genomic diversity

The genomic diversity traced in empirical data from 2020 to 2024 shows fluctuating yet relatively stationary dynamics, without notable trends of increasing or decreasing diversity, as illustrated in Fig. 2 (C)). The Augmented Dicky-Fuller (ADF) test (detailed in Section 4) applied for the empirical genomic diversity produced p-value of 0.024, indicating stationary at the significance level of 0.05.

However, stationarity of the simulated genomic diversity is harder to establish for larger population sizes, as illustrated in Fig. 27. For a small population of 1.7 million, the genomic diversity dynamics are closer to stationary (p-value of 0.078). This outcome is robust to variations of the fitness contributions weight table, as well as changes in the within-host selective pressure, as shown in Fig. 28. For larger population sizes, the ADF tests produced larger p-values of 0.317 (8 million) and 0.730 (25.4 million), indicating a progressive loss of stationarity.

G Sensitivity analysis

We performed sensitivity analysis by tracing the output variables of interest in response to changes in one input variable while keeping the other inputs specified at default values. In this study, we have four output variables of interest: incidence, transmissibility fitness, accumulated mutations, and genomic diversity. Figures 29 and 30 show simulated

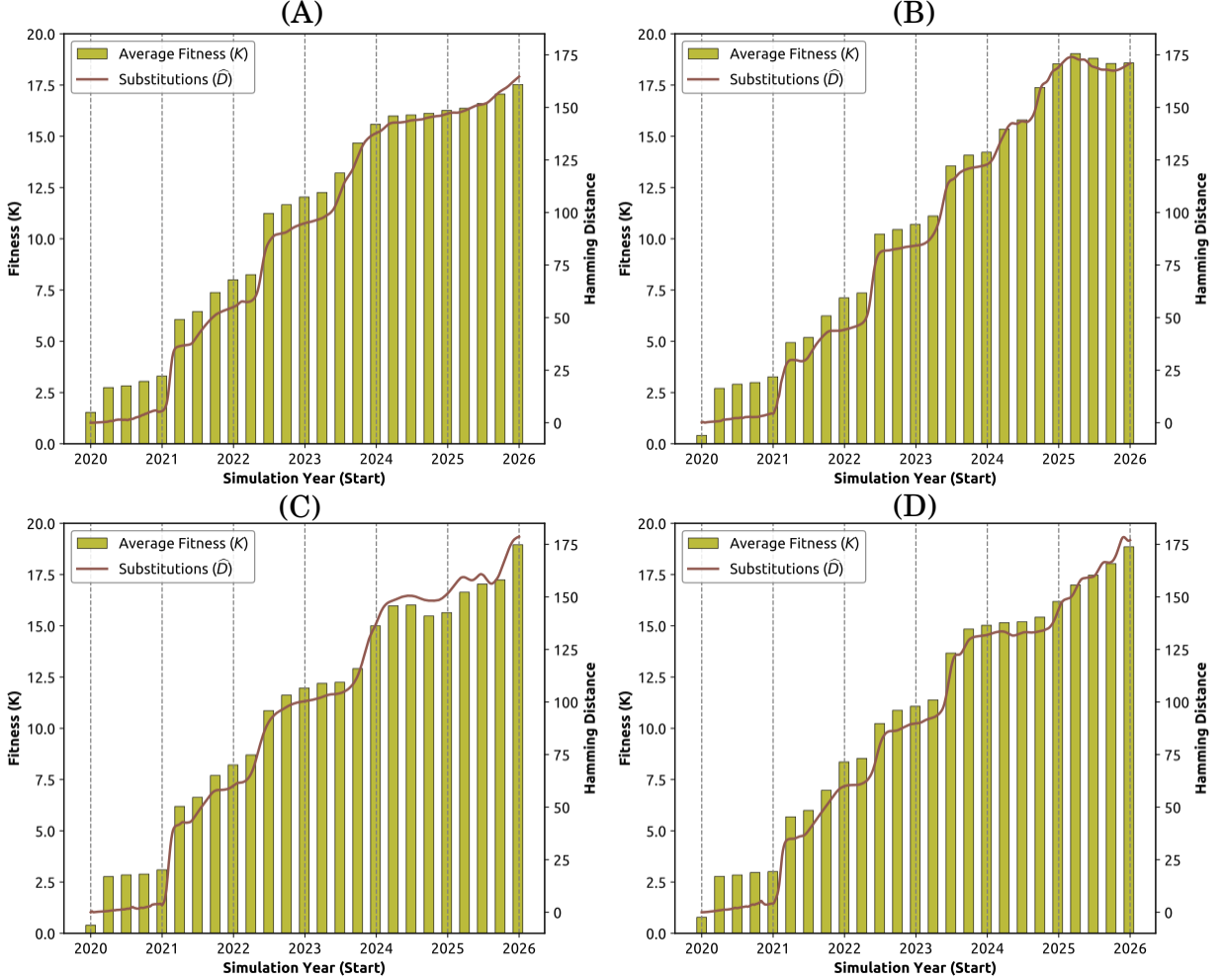


Figure 22: Simulated dynamics of the average transmissibility, i.e., fitness (K , olive bars, y-axis on the left), and the accumulated mutations (\hat{D} , solid brown line, y-axis on the right) for a 25.4 million population from 2020 to 2026. Panels (A)-(D) are profiles plotted using four different realisations.

dynamics of the output variables of interest by varying two input parameters: the fraction of chronically infected hosts and the within-host selective pressure in chronically infected hosts, respectively.

H Computational complexity and implementation

The multi-scale phylodynamic simulator, PHASE TRACE, builds upon our open-source agent-based epidemiological simulator, AMTRaC-19 [57], written in C++. The architecture of PHASE TRACE includes four layers (Fig. 12), with the immunological and phylogenetic layers being novel additions, which significantly extend the capabilities of AMTRaC-19. PHASE TRACE is designed to simulate the dynamic interaction between pathogen transmission and evolution over a prolonged timeframe over multiple years (unlike AMTRaC-19 which was typically used to simulate 6-9 months of a pandemic). The new modelling capabilities and simulation requirements increase the computational complexity, presenting four specific computational challenges:

- *Longer simulation timeframe* (typically, over 6 years or 2,000 simulation days). This is needed to trace the medium-term evolutionary dynamics of pathogens. State-of-the-practice simulators typically employ a short epidemic or pandemic simulation timeframe (e.g., 6-9 months), aiming to examine the short-term impact of public health interventions.

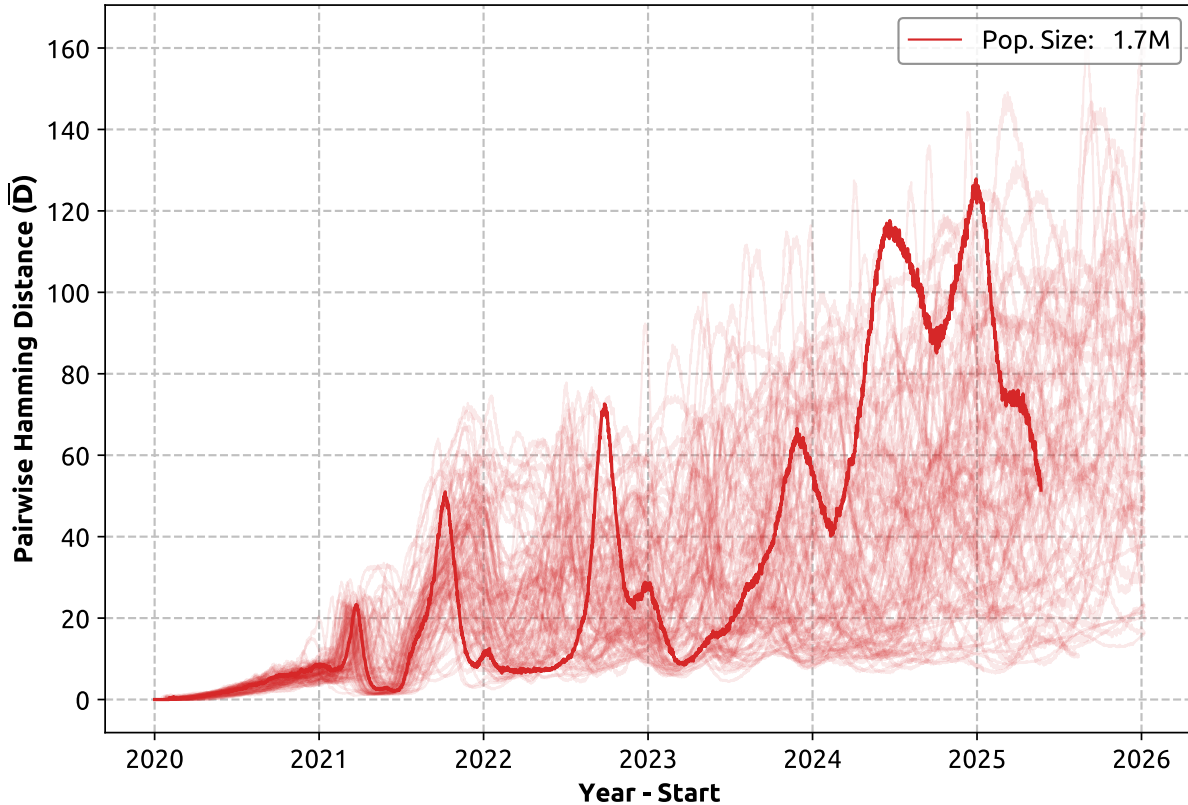


Figure 23: Simulated dynamics of the average pairwise Hamming distance (\bar{D}) between two randomly selected genomes from infected hosts in a population of 1.7 million. Approximately 10,000 pairs of genomes are randomly sampled at each simulation time point from 2020 to 2026 (Capability 2(i)). Opaque red lines represent the ensemble of all realisations and the solid red line shows the dynamics of one realisation only.

- *Compound and waning immunity*, combining both the immunisation and infection histories. This demands higher memory, continually increasing during the simulation as the agents are likely to accumulate multiple vaccination records and infections during the simulated time frame.
- *Complex phylogenetic structure* based on a non-homogeneous genome profile. Each infected agent is assigned a genome profile defined across thousands of nucleotide positions (e.g., 3,090 positions), partitioned between spike and non-spike regions and grouped in terms of antigenicity. Simulation of complex phylodynamics generates a memory-intensive computation task that demands a significant increase in both simulation time and computational resources.
- *Simulation across heterogeneous demographics*, with varying population sizes (including very dense populations). Simulating different demographics is needed to investigate conditions for the emergence of variants of concern (VoC), commonly observed in large heterogeneous populations.

H.1 Performance and scalability

To improve computational efficiency, PHASE TRACE utilises multi-threading processing provided by the C++ OpenMP library. Figure 31 traces the average processing time of simulation runs performed on a high-performance computing cluster, for three different population sizes, ranging from approximately 230,000 agents (Figure 31.A), to approximately 1,700,000 agents (Figure 31.B), and approximately 8,000,000 agents (Figure 31.C).

The average processing time per simulation day increases during the simulation: this occurs due to the increased memory (see the top row of Figure 31). Nevertheless, there is a consistent reduction of the processing time when more CPUs are used per job. We note that, for a given number of CPUs, the average cumulative processing time linearly

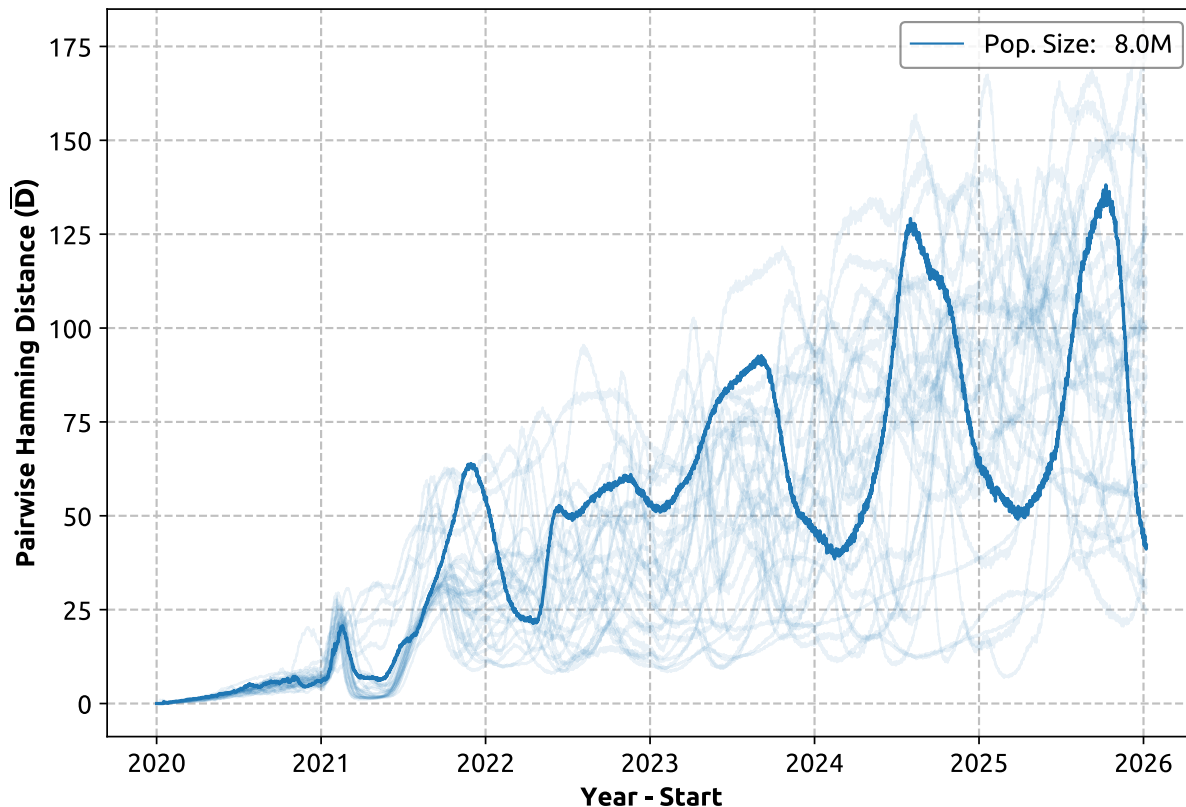


Figure 24: Simulated dynamics of the average pairwise Hamming distance between two randomly selected genomes from infected hosts in a population of 8.0 million. Approximately 10,000 pairs of genomes are randomly sampled at each simulation time point from 2020 to 2026 (Capability 2(i)). Opaque blue lines represent the ensemble of all realisations and the solid blue line shows the dynamics of one realisation only.

increases in proportion to the population size. For example, Figure 32 shows that when 8 CPUs are used, a simulation of a 365-day period across a population with 8 million agents completes in approximately 20,000 seconds (over 5.5 hours).

H.2 Memory utilisation

An increasing size of the artificial population requires higher computation resources. This is because the stochastically generated agents are assigned several static demographic attributes, which are preserved during the simulation, and a number of dynamic phylogenetic and immunological attributes, which change during the simulation. These attributes contribute to both fixed memory and dynamic memory utilisation.

Agent attributes that utilise fixed memory include:

- **Demographic attributes:** household composition and age group.
- **Working group and school enrollment:** workplace for agents over the age of 18, or school for agents under the age of 18.

Agent attributes that affect dynamic memory utilisation during simulation include:

- **Vaccination history:** type of the administered vaccine, the total number of vaccination records and the time of vaccination.

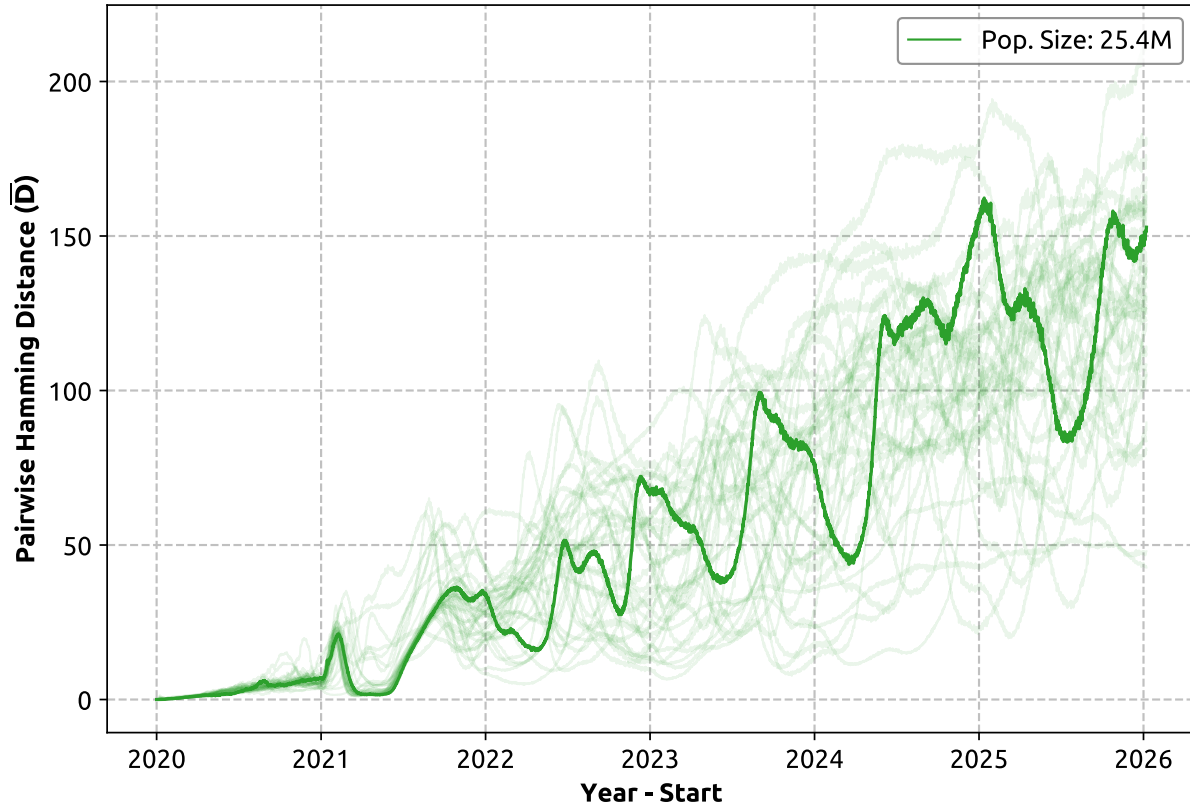


Figure 25: Simulated dynamics of the average pairwise Hamming distance between two randomly selected genomes from infected hosts in a population of 25.4 million. Approximately 10,000 pairs of genomes are randomly sampled at each simulation time point from 2020 to 2026 (Capability 2(i)). Opaque green lines represent the ensemble of all realisations and the solid green line shows the dynamics of one realisation only.

- **Infection history:** the number of past infections and their recovery times.
- **Genome profiles:** infected agents are assigned a genome profile transferred from the source of infection, which continues to mutate during the agent's infectivity period.

As the simulation progresses, the number of stored immunological records grows significantly due to the increased number of infections and administered vaccinations. Figure 33 shows how the dynamic memory usage (in Gigabytes) increases with the larger number of stored immunological records across the population of 8 million agents.

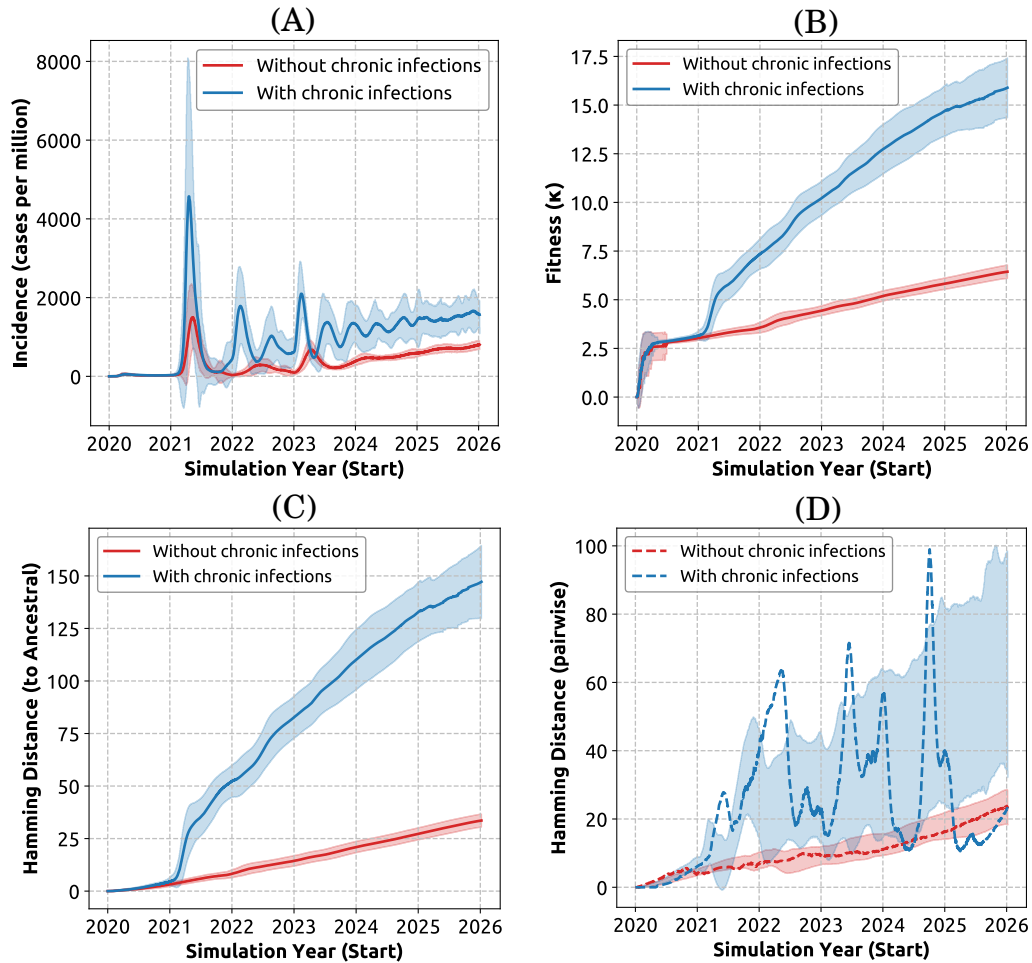


Figure 26: Simulated dynamics in scenarios with the fraction of agents susceptible to chronic infections being 0.1% of the entire population (blue curves), and without chronic infections (red curves). The profiles trace detected (A) incidence, (B) average pathogen transmissibility, interpreted as fitness K , (C) accumulated mutations (\hat{D}), and (D) genomic diversity (\bar{D}) in the population of 1.7 million, over six simulation years. The shaded area represents the range of one standard deviation from the mean values. In (A) to (C), the solid lines denote the mean value across 30-50 realisations. In (D), the dashed line denotes the pairwise Hamming distance from one realisation only, given the high variability between realisations.

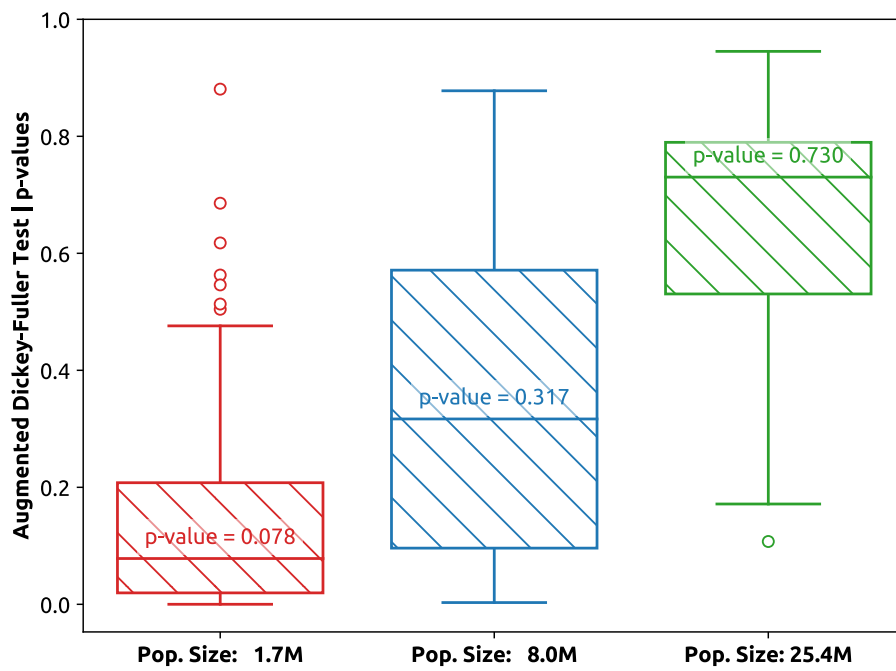


Figure 27: Statistical estimation of stationarity of the time evolution of the average pairwise Hamming distance between two randomly selected genomes. Approximately 10,000 pairs of genome sequences are randomly sampled at each simulation time point from 2020 to 2026 for three simulation scenarios with different population sizes of 1.7 million (A), 8 million (B), and 25.4 million (C) (Capability 3(ii)).

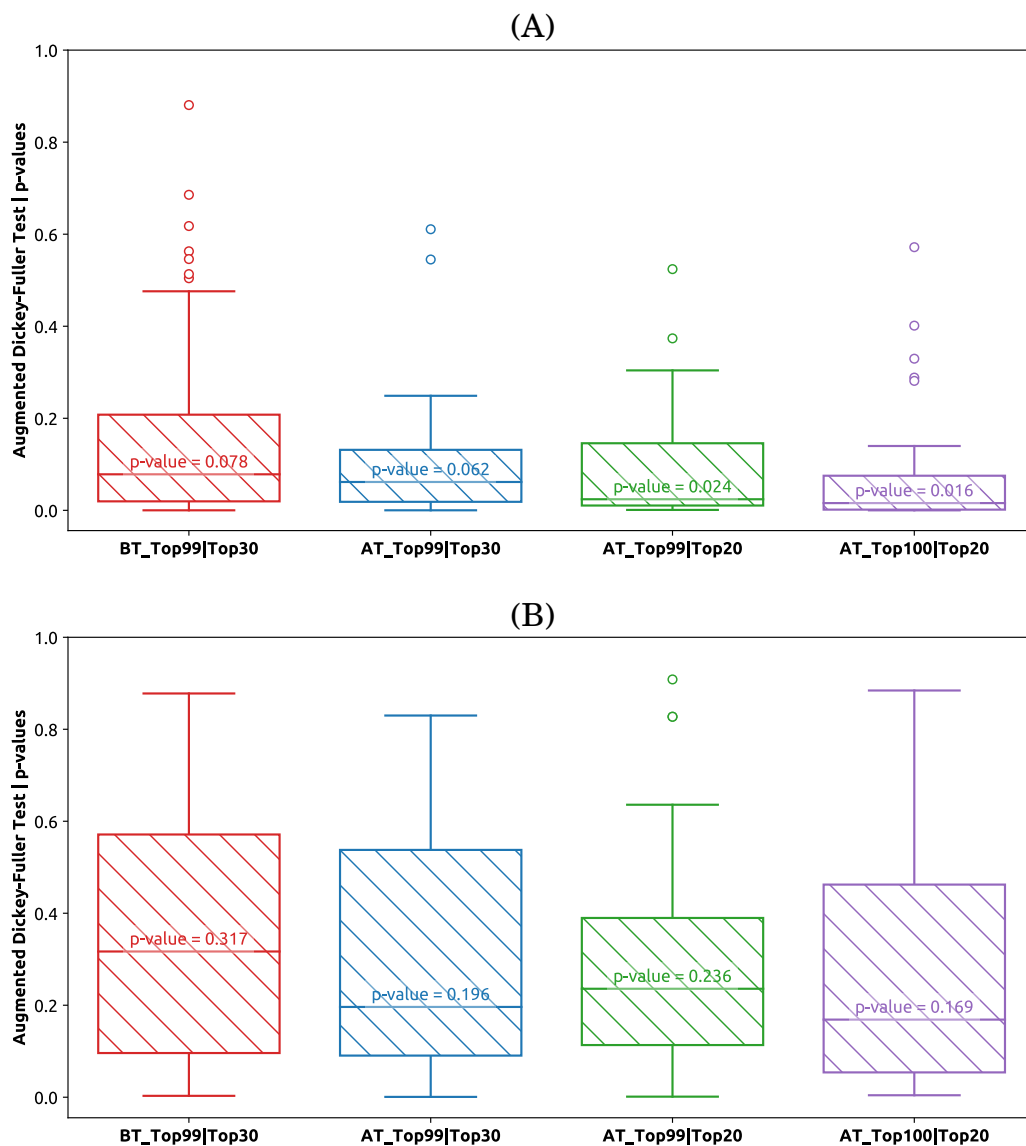


Figure 28: Statistical estimation of the stationarity of the average pairwise Hamming distance between two randomly selected genomes simulated with populations of 1.7 million (A) and 8.0 million (B). Approximately 10,000 pairs of genome sequences are randomly sampled at each simulation time point from 2020 to 2026 for four simulation scenarios by varying amino acid weight table and/or within-host selective pressure (see bar legends). We tested two different fitness weight tables following two different normal distributions: (i) *BT*: the baseline setting, where each amino acid contribution in spike and non-spike codon positions is sampled from the normal distributions $N(0, 0.085)$ and $N(0, 0.07)$, respectively, and (ii) *AT*: the alternative setting, where each amino acid contribution in spike and non-spike codon positions is sampled from the normal distributions $N(0, 0.0489)$ and $N(0, 0.0454)$, respectively. Within-host selective pressure is varied for both typical infected hosts and chronically infected hosts, using notation separated by a vertical bar (e.g., *Top99|Top30* represents a setting where selective pressure at top 99 for typically infected hosts ($X=99, M=100$) and at top 30 for chronically infected hosts ($X=30, M=100$)).

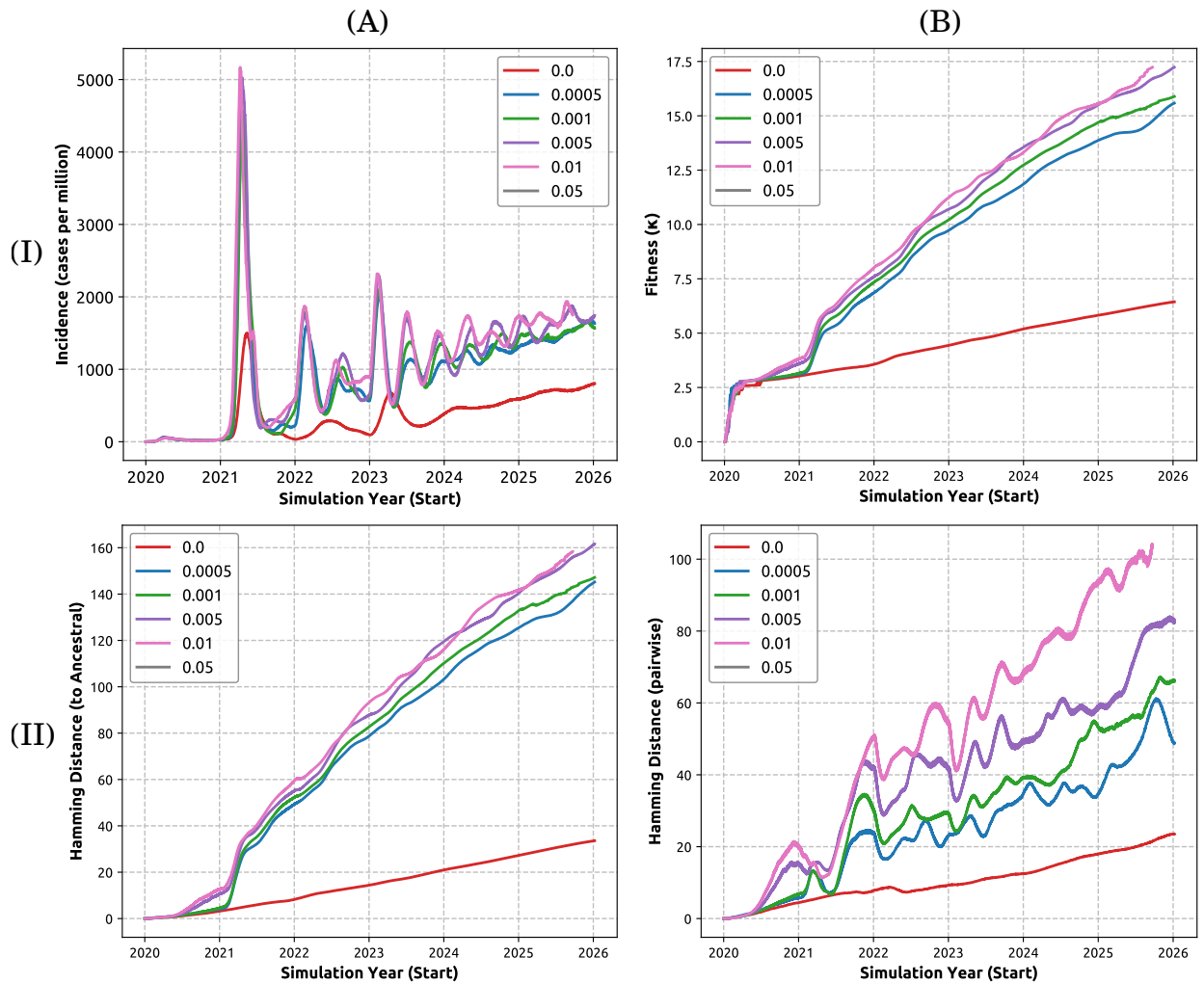


Figure 29: Simulated dynamics of the detected incidence (I-A), average pathogen fitness (I-B), average accumulated mutations \hat{D} (II-A), and average genomic diversity \bar{D} (II-B) in a population of 1.7 million. These measures are traced while the fraction of individuals susceptible to chronic infection, with strong positive within-host selective pressure, is varied from 0.0 to 0.05 of the total population.

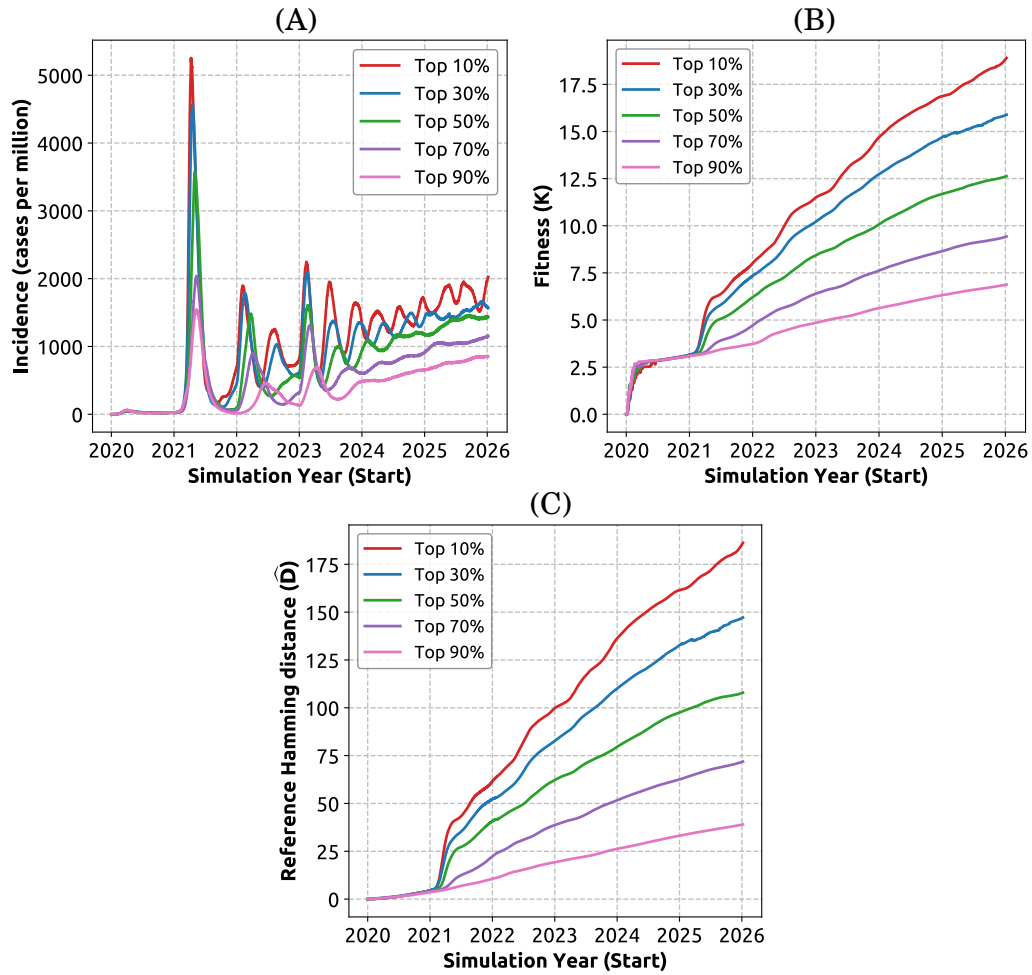


Figure 30: Simulated dynamics of (A) detected incidence, (B) average pathogen fitness, and (C) average accumulated mutations \bar{D} in a population of 1.7 million. The within-host selective pressure for chronically infected hosts, starting from day 60 of infection, is varied by selecting, in each simulation cycle, the mutated genomes from the top 10% (high selectivity, $X = 10$, $M = 100$) to the top 90% (low selectivity, $X = 90$, $M = 100$) of the ranked list of mutated genome candidates.

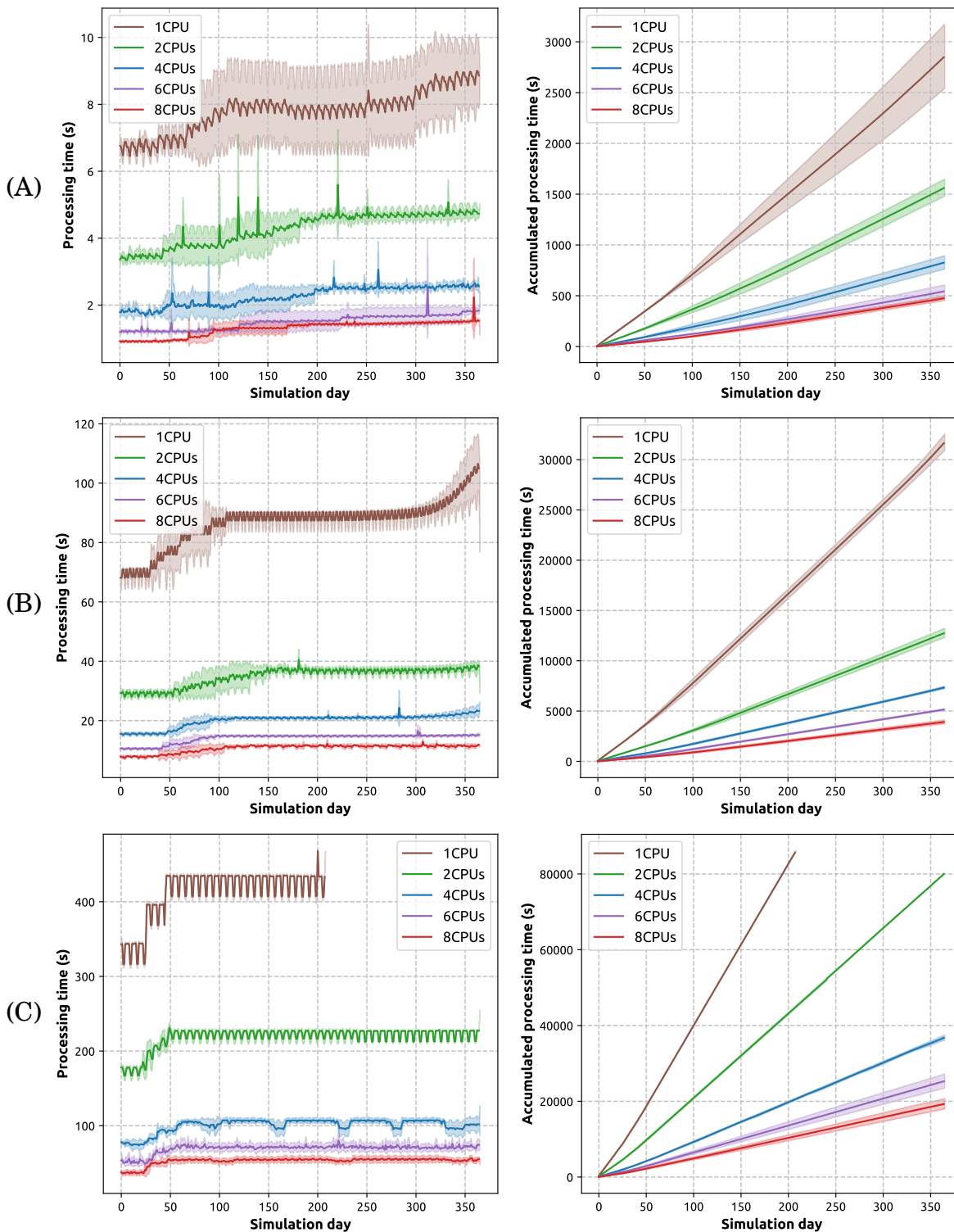


Figure 31: Reduction of the average processing time (seconds) by utilising more CPUs (between 1 and 8). The simulation covers 365 simulation days for three different population sizes: (A) 230K agents, (B) 1.7M agents, and (C) 8M agents. *Left*: the processing time required to simulate a single simulation day. *Right*: the cumulative processing time required to simulate 365 days. Confidence intervals are shown as shaded areas.

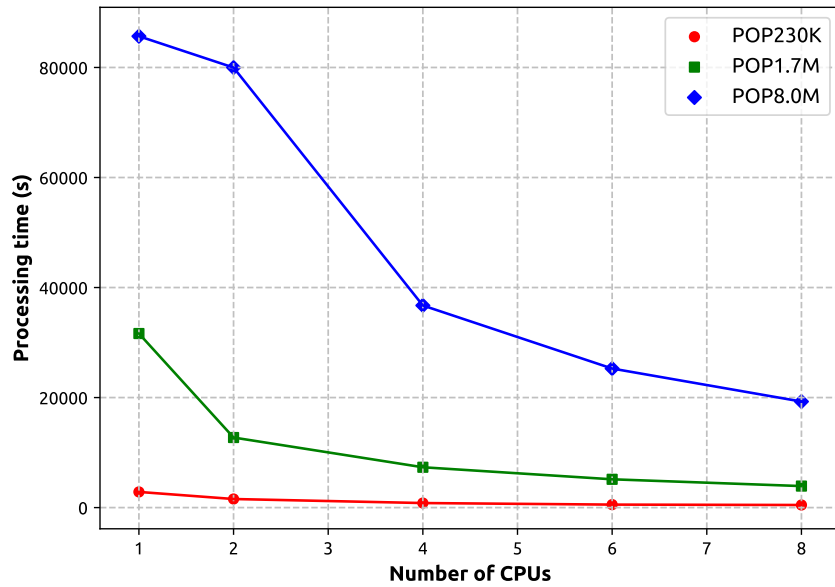


Figure 32: Average cumulative processing time (seconds) for a simulation over 365 days, performed on multiple CPUs in the range between 1 and 8. Population sizes: 230K agents (red), 1.7M agents (green), and 8M agents (blue).

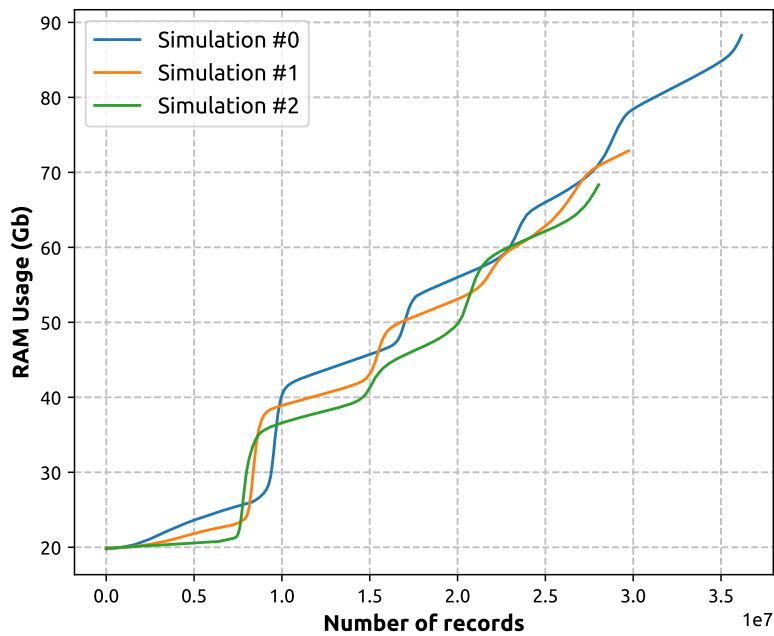


Figure 33: Dependency of the total number of stored immunological records (tens of millions), combining vaccination and infection histories of 8 million agents, and the amount of memory (RAM, Gigabytes) required for a simulation period of 1,200 days. Each profile represents an individual realisation. All realisations are simulated under identical inputs and settings.

References

- [1] Gianluca Fabiani, Nikolaos Evangelou, Tianqi Cui, Juan M. Bello-Rivas, Cristina P. Martin-Linares, Constantinos Siettos, and Ioannis G. Kevrekidis. Task-oriented machine learning surrogates for tipping points of agent-based models. *Nature Communications*, 15(1):4117, May 2024.
- [2] S. Eubank, H. Guclu, V. Anil Kumar, and et al. Modelling disease outbreaks in realistic urban social networks. *Nature*, page 180–184, 2004.
- [3] Timothy C. Germann, Kai Kadau, Ira M. Longini, and Catherine A. Macken. Mitigation strategies for pandemic influenza in the United States. *Proceedings of the National Academy of Sciences*, 103(15):5935–5940, April 2006.
- [4] Elaine O Nsoesie, Richard J Beckman, and Madhav V Marathe. Sensitivity analysis of an individual-based model for simulation of influenza epidemics. *PLOS ONE*, 7(10):0045414, 2012.
- [5] R. J. Rockett and et al. Revealing COVID-19 transmission by SARS-CoV-2 genome sequencing and agent-based modelling. *Nature Medicine*, 26:1398–1404, 2020.
- [6] S. L. Chang and et al. Modelling transmission and control of the COVID-19 pandemic in Australia. *Nat. Commun.*, 11(1):5710, 2020.
- [7] Nick Scott, Anna Palmer, Dominic Delpont, Romesh Abeysuriya, Robyn Stuart, Cliff C Kerr, Dina Mistry, Daniel J Klein, Rachel Sacks-Davis, Katie Heath, et al. Modelling the impact of reducing control measures on the COVID-19 pandemic in a low transmission setting. *Medical Journal of Australia*, 214(2):79–83, 2020.
- [8] Tony Blakely, Jason Thompson, Natalie Carvalho, Laxman Bablani, Nick Wilson, and Mark Stevenson. The probability of the 6-week lockdown in Victoria (commencing 9 July 2020) achieving elimination of community transmission of SARS-CoV-2. *Medical Journal of Australia*, 213(8):349–351, 2020.
- [9] CC Kerr, RM Stuart, D Mistry, RG Abeysuriya, K Rosenfeld, GR Hart, and et al. Covasim: An agent-based model of covid-19 dynamics and interventions. *PLoS Computational Biology*, 17(e1009149), 2021.
- [10] Neil M Ferguson, Daniel Laydon, Gemma Nedjati-Gilani, Natsuko Imai, Kylie Ainslie, Marc Baguelin, Sangeeta Bhatia, Adhiratha Boonyasiri, Zulma Cucunubá, Gina Cuomo-Dannenburg, et al. Impact of non-pharmaceutical interventions (NPIs) to reduce COVID-19 mortality and healthcare demand, 2020.
- [11] World Health Organization Regional Office for the Western Pacific. Calibrating long-term non-pharmaceutical interventions for COVID-19: Principles and facilitation tools, 2021.
- [12] N. Ferguson, A. Galvani, and R. Bush. Ecological and immunological determinants of influenza evolution. *Nature*, 422(428-433), 2003.
- [13] B.F. Nielsen, C.M. Saad-Roy, Y. Li, K. Sneppen, L. Simonsen, C. Viboud, and et al. Host heterogeneity and epistasis explain punctuated evolution of SARS-CoV-2. *PLoS Computational Biology*, 19(2):e1010896, 2023.
- [14] Global Change Data Lab. Coronavirus (COVID-19) Cases.
- [15] James Hadfield, Colin Megill, Sidney M Bell, John Huddleston, Barney Potter, Charlton Callender, Pavel Sagulenko, Trevor Bedford, and Richard A Neher. nCoV full open data.
- [16] Fritz Obermeyer, Martin Jankowiak, Nikolaos Barkas, Stephen F. Schaffner, Jesse D. Pyle, Leonid Yurkovetskiy, Matteo Bosso, Daniel J. Park, Mehrtash Babadi, Bronwyn L. MacInnis, Jeremy Luban, Pardis C. Sabeti, and Jacob E. Lemieux. Analysis of 6.4 million sars-cov-2 genomes identifies mutations associated with fitness. *Science*, 376(6599):1327–1332, 2022.
- [17] James Hadfield, Colin Megill, Sidney M Bell, John Huddleston, Barney Potter, Charlton Callender, Pavel Sagulenko, Trevor Bedford, and Richard A Neher. Genomic epidemiology of sars-cov-2 with subsampling focused globally since pandemic start.
- [18] O. M. Cliff, M. Harding, M. Piraveen, Y. Erten, M. Gambhir, and M. Prokopenko. Investigating spatiotemporal dynamics and synchrony of influenza epidemics in Australia: an agent-based modelling approach. *Simulation Modelling Practice and Theory*, 87:412–431, 2018.
- [19] Cameron Zachreson, Kristopher M Fair, Oliver M Cliff, Nathan Harding, Mahendra Piraveenan, and Mikhail Prokopenko. Urbanization affects peak timing, prevalence, and bimodality of influenza pandemics in australia: results of a census-calibrated model. *Science advances*, 4(12):eaau5294, 2018.
- [20] Cameron Zachreson, Kristopher M Fair, Nathan Harding, and Mikhail Prokopenko. Interfering with influenza: nonlinear coupling of reactive and static mitigation strategies. *Journal of The Royal Society Interface*, 17(165):20190728, 2020.
- [21] S. L. Chang and et al. AMTraC-19 Source Code: Agent-based Model of Transmission and Control of the COVID-19 pandemic in Australia.

- [22] C. Zachreson and et al. How will mass-vaccination change COVID-19 lockdown requirements in Australia? *The Lancet Regional Health - Western Pacific*, 14:100224, September 2021.
- [23] S. L. Chang and et al. Simulating Transmission Scenarios of the Delta Variant of SARS-CoV-2 in Australia. *Front. Public Health*, 10, 2022.
- [24] Q. D. Nguyen, S. L. Chang, C. M. Jamerlan, and M. Prokopenko. Measuring unequal distribution of pandemic severity across census years, variants of concern and interventions. *Population Health Metrics*, 21(17):17.
- [25] Kristopher M. Fair, Cameron Zachreson, and Mikhail Prokopenko. Creating a surrogate commuter network from Australian Bureau of Statistics census data. *Scientific Data*, 6(1):150, August 2019.
- [26] S. L. Chang and et al. Persistence of the Omicron variant of SARS-CoV-2 in Australia: The impact of fluctuating social distancing. *PLOS Global Public Health*, 3(4):e0001427, April 2023.
- [27] Sheryl L. Chang, Quang Dang Nguyen, Carl J. E. Suster, Christina M. Jamerlan, Rebecca J. Rockett, Vitali Sintchenko, Tania C. Sorrell, Alexandra Martiniuk, and Mikhail Prokopenko. Impact of opinion dynamics on recurrent pandemic waves: balancing risk aversion and peer pressure, 2024.
- [28] Remco Bouckaert, Timothy G. Vaughan, Joëlle Barido-Sottani, Sebastián Duchêne, Mathieu Fourment, Alexandra Gavryushkina, Joseph Heled, Graham Jones, Denise Kühnert, Nicola De Maio, Michael Matschiner, Fábio K. Mendes, Nicola F. Müller, Huw A. Ogilvie, Louis du Plessis, Alex Poppinga, Andrew Rambaut, David Rasmussen, Igor Siveroni, Marc A. Suchard, Chieh-Hsi Wu, Dong Xie, Chi Zhang, Tanja Stadler, and Alexei J. Drummond. BEAST 2.5: An advanced software platform for Bayesian evolutionary analysis. *PLOS Computational Biology*, 15(4):e1006650, April 2019.
- [29] Bas B. Oude Munnink, David F. Nieuwenhuijse, Mart Stein, Aine O’Toole, Manon Haverkate, Madelief Mollers, Sandra K. Kamga, Claudia Schapendonk, Mark Pronk, Pascal Lexmond, Anne van der Linden, Theo Bestebroer, Irina Chestakova, Ronald J. Overmars, Stefan van Nieuwkoop, Richard Molenkamp, Annemiek A. van der Eijk, Corine GeurtsvanKessel, Harry Vennema, Adam Meijer, Andrew Rambaut, Jaap van Dissel, Reina S. Sikkema, Aura Timen, and Marion Koopmans. Rapid SARS-CoV-2 whole-genome sequencing and analysis for informed public health decision-making in the Netherlands. *Nature Medicine*, 26(9):1405–1410, September 2020.
- [30] Ivica Letunic and Peer Bork. Interactive Tree of Life (iTOL) v6: recent updates to the phylogenetic tree display and annotation tool. *Nucleic Acids Research*, 52(W1):W78–W82, July 2024.
- [31] Peter V. Markov, Mahan Ghafari, Martin Beer, Katrina Lythgoe, Peter Simmonds, Nikolaos I. Stilianakis, and Aris Katzourakis. The evolution of SARS-CoV-2. *Nature Reviews Microbiology*, 21(6):361–379, June 2023.
- [32] Australian Bureau of Statistics. 2021 Census of Population and Housing. Accessed on 01 December 2022.
- [33] Lindell Bromham. Why do species vary in their rate of molecular evolution? *Biology Letters*, 5(3):401–404, June 2009.
- [34] Soojin. Yi. Neutrality and Molecular Clocks. *Nature Education Knowledge*, 4(3), 2013.
- [35] Aluísio Pinheiro, Hildete Prisco Pinheiro, and Pranab Kumar Sen. The use of hamming distance in bioinformatics. In Ranajit Chakraborty, C.R. Rao, and Pranab Sen, editors, *Handbook of Statistics*, volume 28, pages 129–162. Elsevier, 2012.
- [36] F. Wu, S. Zhao, B. Yu, and et al. A new coronavirus associated with human respiratory disease in China. *Nature*, page 265–269, 2020.
- [37] David A. Dickey and Wayne A. Fuller. Distribution of the Estimators for Autoregressive Time Series With a Unit Root. *Journal of the American Statistical Association*, 74(366):427, June 1979.
- [38] E. S. Page. CONTINUOUS INSPECTION SCHEMES. *Biometrika*, 41(1-2):100–115, 1954.
- [39] Sheldon M. Ross. Chapter 13 - Quality Control. In Sheldon M. Ross, editor, *Introduction to Probability and Statistics for Engineers and Scientists (Fifth Edition)*, pages 553–587. Academic Press, Boston, January 2014.
- [40] Ann P. Smith. Nucleic acids to amino acids: DNA specifies protein. *Nature Education*, 1(1):126.
- [41] William T. Harvey, Alessandro M. Carabelli, Ben Jackson, Ravindra K. Gupta, Emma C. Thomson, Ewan M. Harrison, Catherine Ludden, Richard Reeve, Andrew Rambaut, Sharon J. Peacock, and David L. Robertson. SARS-CoV-2 variants, spike mutations and immune escape. *Nature Reviews Microbiology*, 19(7):409–424, July 2021.
- [42] Christof C. Smith, Kelly S. Olsen, Kaylee M. Gentry, Maria Sambade, Wolfgang Beck, Jason Garness, Sarah Entwistle, Caryn Willis, Steven Vensko, Allison Woods, Misha Fini, Brandon Carpenter, Eric Routh, Julia Kodysh, Timothy O’Donnell, Carsten Haber, Kirsten Heiss, Volker Stadler, Erik Garrison, Adam M. Sandor, Jenny P. Y. Ting, Jared Weiss, Krzysztof Krajewski, Oliver C. Grant, Robert J. Woods, Mark Heise, Benjamin G. Vincent, and

- Alex Rubinsteyn. Landscape and selection of vaccine epitopes in SARS-CoV-2. *Genome Medicine*, 13(1):101, June 2021.
- [43] Ron Sender, Yinon M. Bar-On, Shmuel Gleizer, Biana Bernshtein, Avi Flamholz, Rob Phillips, and Ron Milo. The total number and mass of SARS-CoV-2 virions. *Proceedings of the National Academy of Sciences*, 118(25):e2024815118, June 2021.
- [44] Kathryn E. Kistler, John Huddleston, and Trevor Bedford. Rapid and parallel adaptive mutations in spike S1 drive clade success in SARS-CoV-2. *Cell Host & Microbe*, 30(4):545–555.e4, April 2022.
- [45] Nicole N. Thadani, Sarah Gurev, Pascal Notin, Noor Youssef, Nathan J. Rollins, Daniel Ritter, Chris Sander, Yarin Gal, and Debora S. Marks. Learning from pre-pandemic data to forecast viral escape. *Nature*, 622(7984):818–825, October 2023.
- [46] Mahan Ghafari, Matthew Hall, Tanya Golubchik, Daniel Ayoubkhani, Thomas House, George MacIntyre-Cockett, Helen R. Fryer, Laura Thomson, Anel Nurtay, Steven A. Kemp, Luca Ferretti, David Buck, Angie Green, Amy Trebes, Paolo Piazza, Lorne J. Lonie, Ruth Studley, Emma Rourke, Darren L. Smith, Matthew Bashton, Andrew Nelson, Matthew Crown, Clare McCann, Gregory R. Young, Rui Andre Nunes dos Santos, Zack Richards, Mohammad Adnan Tariq, Roberto Cahuantzi, Jeff Barrett, Christophe Fraser, David Bonsall, Ann Sarah Walker, and Katrina Lythgoe. Prevalence of persistent SARS-CoV-2 in a large community surveillance study. *Nature*, 626(8001):1094–1101, February 2024.
- [47] Massimo Amicone, Vítor Borges, Maria João Alves, Joana Isidro, Líbia Zé-Zé, Sílvia Duarte, Luís Vieira, Raquel Guiomar, João Paulo Gomes, and Isabel Gordo. Mutation rate of SARS-CoV-2 and emergence of mutators during experimental evolution. *Evolution, Medicine, and Public Health*, 10(1):142–155, January 2022.
- [48] Stephen W. Attwood, Sarah C. Hill, David M. Aanensen, Thomas R. Connor, and Oliver G. Pybus. Phylogenetic and phylodynamic approaches to understanding and combating the early SARS-CoV-2 pandemic. *Nature Reviews Genetics*, 23(9):547–562, September 2022.
- [49] Jialin Yang, Michael Skaro, Jiani Chen, Duna Zhan, Leke Lyu, Skylar Gay, Ahmed Kandeil, Mohamed A. Ali, Ghazi Kayali, Kateryna Stoianova, Pensheng Ji, Magdy Alabady, Justin Bahl, Liang Liu, and Jonathan Arnold. The species coalescent indicates possible bat and pangolin origins of the COVID-19 pandemic. *Scientific Reports*, 13(1):5571, April 2023.
- [50] Rowena A. Bull, John-Sebastian Eden, Fabio Luciani, Kerensa McElroy, William D. Rawlinson, and Peter A. White. Contribution of Intra- and Interhost Dynamics to Norovirus Evolution. *Journal of Virology*, 86(6):3219–3229, March 2012.
- [51] Carolina M Voloch, Ronaldo Da Silva Francisco Jr, Luiz G P De Almeida, Otavio J Brustolini, Cynthia C Cardoso, Alexandra L Gerber, Ana Paula De C Guimarães, Isabela De Carvalho Leitão, Diana Mariani, Victor Akira Ota, Cristiano X Lima, Mauro M Teixeira, Ana Carolina F Dias, Rafael Mello Galliez, Débora Souza Faffe, Luís Cristóvão Pôrto, Renato S Aguiar, Terezinha M P P Castiñeira, Orlando C Ferreira, Amilcar Tanuri, and Ana Tereza R De Vasconcelos. Intra-host evolution during SARS-CoV-2 prolonged infection. *Virus Evolution*, 7(2):veab078, December 2021.
- [52] Ana S. Gonzalez-Reiche, Hala Alshammary, Sarah Schaefer, Gopi Patel, Jose Polanco, Juan Manuel Carreño, Angela A. Amoako, Aria Rooker, Christian Cognigni, Daniel Floda, Adriana van de Guchte, Zain Khalil, Keith Farrugia, Nima Assad, Jian Zhang, Bremy Albuquerque, Levy A. Sominsky, Charles Gleason, Komal Srivastava, Robert Sebra, Juan David Ramirez, Radhika Banu, Paras Shrestha, Florian Krammer, Alberto Paniz-Mondolfi, Emilia Mia Sordillo, Viviana Simon, and Harm van Bakel. Sequential intrahost evolution and onward transmission of SARS-CoV-2 variants. *Nature Communications*, 14(1):3235, June 2023.
- [53] S A J Wilkinson, Alex Richter, Anna Casey, Husam Osman, Jeremy D Mirza, Joanne Stockton, Josh Quick, Liz Ratcliffe, Natalie Sparks, Nicola Cumley, Radoslaw Poplawski, Samuel N Nicholls, Beatrix Kele, Kathryn Harris, Thomas P Peacock, and Nicholas J Loman. Recurrent SARS-CoV-2 mutations in immunodeficient patients. *Virus Evolution*, 8(2):veac050, August 2022.
- [54] Sam Wilkinson. Dataset for “recurrent SARS-CoV-2 mutations in immunodeficient patients”.
- [55] Bureau of Infrastructure and Transport Research Economics. Airport traffic data (2022), August. Accessed on 01 December 2022.
- [56] Australian Curriculum, Assessment and Authority (ACARA). School profiles and locations. Accessed on 01 December 2022.
- [57] Sheryl L. Chang, Quang D. Nguyen, Cameron Zachreson, Oliver M. Cliff, and Mikhail Prokopenko. AMTraC-19 Source Code: Agent-based Model of Transmission and Control of the COVID-19 pandemic in Australia.

- [58] Center for Disease Control and Prevention. What is COVID-19 Reinfection? <https://www.cdc.gov/coronavirus/2019-ncov/your-health/reinfection.html>, 2023.
- [59] New South Wales Health. NSW Respiratory Surveillance Report - week ending 30 July 2022. <https://www.health.nsw.gov.au/Infectious/covid-19/Documents/weekly-covid-overview-20220730.pdf>, 2022.
- [60] CDC. About Chronic Symptoms Following Infections. <https://www.cdc.gov/chronic-symptoms-following-infections/about/>, 2023. accessed on 12 July 2024.
- [61] Cheryl Lin, Brooke Bier, Rungting Tu, John J. Paat, and Pikuei Tu. Vaccinated Yet Booster-Hesitant: Perspectives from Boosted, Non-Boosted, and Unvaccinated Individuals. *Vaccines*, 11(3):550, February 2023.
- [62] Lirong Cao, Jingzhi Lou, See Yeung Chan, Hong Zheng, Caiqi Liu, Shi Zhao, Qi Li, Chris Ka Pun Mok, Renee Wan Yi Chan, Marc Ka Chun Chong, William Ka Kei Wu, Zigui Chen, Eliza Lai Yi Wong, Paul Kay Sheung Chan, Benny Chung Ying Zee, Eng Kiong Yeoh, and Maggie Haitian Wang. Rapid evaluation of COVID-19 vaccine effectiveness against symptomatic infection with SARS-CoV-2 variants by analysis of genetic distance. *Nature Medicine*, 28(8):1715–1722, August 2022.
- [63] J. Szanyi and et al. A log-odds system for waning and boosting of COVID-19 vaccine effectiveness. *Vaccine*, 40(28):3821–3824, 2022.
- [64] Howard Larkin. Hybrid Immunity More Protective Than Prior SARS-CoV-2 Infection Alone. *JAMA*, 329(7):531, February 2023.
- [65] World Health Organization. Interim statement on hybrid immunity and increasing population seroprevalence rates.
- [66] Lanying Du, Yuxian He, Yusen Zhou, Shuwen Liu, Bo-Jian Zheng, and Shibo Jiang. The spike protein of SARS-CoV — a target for vaccine and therapeutic development. *Nature Reviews Microbiology*, 7(3):226–236, March 2009.
- [67] S. Cankat, M. U. Demael, and L. Swadling. In search of a pan-coronavirus vaccine: next-generation vaccine design and immune mechanisms. *Cellular & Molecular Immunology*, 21(2):103–118, February 2024.
- [68] Noah Kojima and Jeffrey D Klausner. Protective immunity after recovery from SARS-CoV-2 infection. *The Lancet Infectious Diseases*, 22(1):12–14, January 2022.
- [69] Sachiko Kodera, Essam A. Rashed, and Akimasa Hirata. Estimation of Real-World Vaccination Effectiveness of mRNA COVID-19 Vaccines against Delta and Omicron Variants in Japan. *Vaccines*, 10(3):430, March 2022.
- [70] Deborah Cromer, Megan Steain, Arnold Reynaldi, Timothy E. Schlub, Shanchita R. Khan, Sarah C. Sasson, Stephen J. Kent, David S. Khoury, and Miles P. Davenport. Predicting vaccine effectiveness against severe COVID-19 over time and against variants: a meta-analysis. *Nature Communications*, 14(1):1633, March 2023.
- [71] Cristina Menni, Anna May, Lorenzo Polidori, Panayiotis Louca, Jonathan Wolf, Joan Capdevila, Christina Hu, Sebastien Ourselin, Claire J Steves, Ana M Valdes, and Tim D Spector. COVID-19 vaccine waning and effectiveness and side-effects of boosters: a prospective community study from the ZOE COVID Study. *The Lancet Infectious Diseases*, 22(7):1002–1010, July 2022.
- [72] David S. Khoury, Deborah Cromer, Arnold Reynaldi, Timothy E. Schlub, Adam K. Wheatley, Jennifer A. Juno, Kanta Subbarao, Stephen J. Kent, James A. Triccas, and Miles P. Davenport. Neutralizing antibody levels are highly predictive of immune protection from symptomatic SARS-CoV-2 infection. *Nature Medicine*, 27(7):1205–1211, July 2021.
- [73] Francesco Menegale, Mattia Manica, Agnese Zardini, Giorgio Guzzetta, Valentina Marziano, Valeria d’Andrea, Filippo Trentini, Marco Ajelli, Piero Poletti, and Stefano Merler. Evaluation of Waning of SARS-CoV-2 Vaccine-Induced Immunity: A Systematic Review and Meta-analysis. *JAMA Network Open*, 6(5):e2310650, May 2023.
- [74] Anyin Feng, Uri Obolski, Lewi Stone, and Daihai He. Modelling COVID-19 vaccine breakthrough infections in highly vaccinated Israel—The effects of waning immunity and third vaccination dose. *PLOS Global Public Health*, 2(11):e0001211, November 2022.
- [75] Ross J. Harris, Jennifer A. Hall, Asad Zaidi, Nick J. Andrews, J. Kevin Dunbar, and Gavin Dabrera. Effect of Vaccination on Household Transmission of SARS-CoV-2 in England. *New England Journal of Medicine*, 385(8):759–760, August 2021.
- [76] Quang Dang Nguyen and Mikhail Prokopenko. A general framework for optimising cost-effectiveness of pandemic response under partial intervention measures. *Scientific Reports*, 12(1):19482, November 2022.

- [77] Nabin K. Shrestha, Patrick C. Burke, Amy S. Nowacki, Paul Terpeluk, and Steven M. Gordon. Necessity of Coronavirus Disease 2019 (COVID-19) Vaccination in Persons Who Have Already Had COVID-19. *Clinical Infectious Diseases: An Official Publication of the Infectious Diseases Society of America*, 75(1):e662–e671, August 2022.
- [78] Nabin K Shrestha, Priyanka Shrestha, Patrick C Burke, Amy S Nowacki, Paul Terpeluk, and Steven M Gordon. Coronavirus Disease 2019 Vaccine Boosting in Previously Infected or Vaccinated Individuals. *Clinical Infectious Diseases*, 75(12):2169–2177, December 2022.
- [79] Matteo Franchi, Giacomo Pellegrini, Danilo Cereda, Francesco Bortolan, Olivia Leoni, Giovanni Pavesi, Massimo Galli, Giuseppina Valenti, and Giovanni Corrao. Natural and vaccine-induced immunity are equivalent for the protection against SARS-CoV-2 infection. *Journal of Infection and Public Health*, 16(8):1137–1141, August 2023.